

3D KINETIC PULSAR MAGNETOSPHERE MODELS:
EXPLORING SELF CONSISTENCY

CONSTANTINOS KALAPOTHARAKOS

University of Maryland, College Park (UMCP/CRESST), College Park, MD 20742, USA and
Astrophysics Science Division, NASA/Goddard Space Flight Center, Greenbelt, MD 20771, USA

GABRIELE BRAMBILLA

Dipartimento di Fisica, Università degli Studi di Milano, Via Celoria 16, 20133 Milano, Italy
Astrophysics Science Division, NASA/Goddard Space Flight Center, Greenbelt, MD 20771, USA and
Istituto Nazionale di Fisica Nucleare, sezione di Milano, Via Celoria 16, 20133 Milano, Italy

ANDREY TIMOKHIN

University of Maryland, College Park (UMCP/CRESST), College Park, MD 20742, USA and
Astrophysics Science Division, NASA/Goddard Space Flight Center, Greenbelt, MD 20771, USA

ALICE K. HARDING

Astrophysics Science Division, NASA/Goddard Space Flight Center, Greenbelt, MD 20771, USA

DEMOSTHENES KAZANAS

Astrophysics Science Division, NASA/Goddard Space Flight Center, Greenbelt, MD 20771, USA
Draft version February 15, 2022

ABSTRACT

We present 3D global kinetic pulsar magnetosphere models, where the charged particle trajectories and the corresponding electromagnetic fields are treated self-consistently. For our study, we have developed a cartesian 3D relativistic particle-in-cell code that incorporates the radiation reaction forces. We describe our code and discuss the related technical issues, treatments, and assumptions. Injecting particles up to large distances in the magnetosphere, we apply arbitrarily low to high particle injection rates and get an entire spectrum of solutions from close to the Vacuum-Retarded-Dipole to close to the Force-Free solution, respectively. For high particle injection rates (close to FF solutions) significant accelerating electric field components are confined only near the equatorial current sheet outside the light-cylinder. The self-consistent nature of our models and a judicious interpretation of them allow the calculation of the particle emission and consequently the derivation of the corresponding realistic high-energy sky-maps and spectra. Using model parameters that cover the entire range of spin-down powers of *Fermi* young and millisecond pulsars, we compare the corresponding model γ -ray light-curves, cutoff energies, and total γ -ray luminosities with those observed by *Fermi* to discover a dependence of the particle injection-rate, \mathcal{F} , on the spin-down power, \dot{E} , indicating an increase of \mathcal{F} with \dot{E} . Our models guided by *Fermi* observations provide field-structures and particle distributions that are not only consistent with each other but also able to reproduce a broad range of the observed γ -ray phenomenology of both young and millisecond pulsars.

Keywords: pulsars: general—stars: neutron—Gamma rays: stars

1. INTRODUCTION

It has been half a century since the first pulsar was observed (Hewish et al. 1968). Pulsars are identified as rapidly rotating Neutron Stars (NS) with huge surface magnetic fields B_* that reach up to $\approx 10^{14}G$. However, they continuously lose rotational energy while they radiate over almost the entire spectrum (from radio to γ -rays). The corresponding brightness temperature of radio emission is extremely high ($10^{23} - 10^{25}K$) indicating its coherent nature. The exact mechanism of radio emission remains unknown although it is believed that it is related to the pair production processes.

However, the radio emission is energetically unimportant in comparison to the high-energy (e.g. γ -rays) emission. For decades we had very limited information about the pulsar γ -ray emission and only after the launch of *Fermi* in 2008 we gained gradually access to a plethora of observational data. Thus, now we have more than 205 detected γ -ray pulsars (117 of them are compiled in the second pulsar catalog (2PC); Abdo et al. 2013) which led to the derivation of meaningful statistical trends and correlations. This introduced the *Fermi*-era in pulsar research affecting significantly the theoretical modeling of the pulsar high-energy emission.

Pulsars are considered to be spherical perfect conductors that rotate within their own magnetic fields. This rotation polarizes the charges, supporting an electric field

inside the conductor star,

$$\mathbf{E} = -\frac{1}{c}(\boldsymbol{\Omega} \times \mathbf{r}) \times \mathbf{B} \quad (1)$$

where Ω is the angular frequency of the star. Assuming a dipole magnetic field and no charges outside the stellar surface the field structure is provided by the analytic Vacuum Retarded Dipole (VRD) solution; (Deutsch 1955).

Early after the discovery of pulsars it became evident that the huge voltages due to the accelerating electric field components \mathbf{E}_{acc} , that exist in VRD solutions, are able to initiate pair cascade processes (Sturrock 1971). Actually, it is believed that the high pair creation efficiency (especially of the $\mathbf{B} - \gamma$ process) would short-out \mathbf{E}_{acc} everywhere in the magnetosphere leading to the so called Force-Free (FF) regime. Thus, pulsars' radiation can be interpreted as the result of their (not totally successful) efforts to construct perfect (conductive) wires using their huge fields and the microphysical processes.

Even though the main principles of the FF solutions had been described in the late 60's and early 70's (e.g. Goldreich & Julian 1969; Scharlemann & Wagoner 1973) the first realistic FF solution for pulsar magnetospheres was presented only two decades ago.

Contopoulos, Kazanas, & Fendt (1999) presented the first FF solution with dipolar magnetic field for the aligned rotator ($\alpha = 0^\circ$, where α is the inclination angle; see also Gruzinov 2005; Timokhin 2006; Komissarov 2006; McKinney 2006; Parfrey et al. 2012; Cao et al. 2016) and Spitkovsky (2006) for the oblique rotator (see also Kalapotharakos & Contopoulos 2009; Pétri 2012b; Tchekhovskoy et al. 2013), respectively. These solutions provided not only the field structure but also the corresponding current and charge densities and revealed that the current closure is achieved by the return current, the main part of it flowing along the equatorial current sheet (ECS) outside the light-cylinder. The ECS is stable up to large distances (Kalapotharakos, Contopoulos, & Kazanas 2012a) while its 3D shape is close to the solution for the current sheet of a FF split monopole solution (Bogovalov 1999).

The FF solutions reveal the currents and field structure that make $\mathbf{E}_{\text{acc}} = 0$ everywhere in the magnetosphere. However, due to their ideal character, they do not provide any information about the acceleration regions, the corresponding emission, and apparently the related \mathbf{E}_{acc} . The only way to study the high-energy emission in FF models was to place arbitrarily the emission regions based on the pulsar radiation models. *Fermi* observations of the high-energy cutoff in the spectrum of the Vela pulsar (Abdo et al. 2009), ruled out polar cap emission models (Arons & Scharlemann 1979; Daugherty & Harding 1982, 1996), which would produce a super-exponential spectral cutoff from magnetic pair attenuation. Thus, the candidate accelerating regions were either (i) along the last open field line, like the Slot Gap (SG) (Arons 1983; Muslimov & Harding 2003, 2004), or (ii) near the Outer Gap (OG) region (Cheng et al. 1986; Romani 1996; Hirotani & Shibata 2001), or (iii) in the ECS (Lyubarskii 1996; Bai & Spitkovsky 2010; Contopoulos & Kalapotharakos 2010; Pétri 2012a; Arka & Dubus 2013) and also (iv) the striped pulsar wind (Pétri & Kirk 2005).

Kalapotharakos et al. (2012c), Li et al. (2012), and more recently Cao et al. (2016), motivated by the aforementioned limitations of the FF solutions, started exploring resistive/dissipative solutions. These models, using rather simple macroscopic prescriptions for the current-density \mathbf{J} , regulate the \mathbf{E}_{acc} through a macroscopic conductivity σ . Varying σ from 0 to ∞ an entire spectrum of solutions from VRD to FF is produced, respectively. The physical meaning of σ is supposedly related to the local pair multiplicity and its efficiency to “kill” \mathbf{E}_{acc} .

These dissipative solutions provided the spatial distribution of \mathbf{E}_{acc} and therefore, allowed for the integration of test particle trajectories in these models and consequently the study of the corresponding emission. Thus, assuming emission due to curvature radiation (CR), Kalapotharakos et al. (2012b) produced the first γ -ray light-curves based on dissipative solutions while Kalapotharakos et al. (2014) found that a hybrid conductivity model that has infinite σ within the light-cylinder (LC) and high and finite σ outside the LC reproduced the radio-lag δ vs. peak-separation Δ correlation shown in 2PC. In the so-called FIDO (FF Inside, Dissipative Outside) models, the emission is produced near the ECS, though the emissivity is not uniformly distributed.

The successful fit of the 2PC $\delta - \Delta$ correlation gave confidence that the FIDO macroscopic models provide viable γ -ray emission geometries. However, a successful high-energy emission model should be able to reproduce the observed spectral properties. Thus, in Brambilla et al. (2015), we used the FIDO models with approximate E_{acc} -values at low σ in order to fit eight bright-pulsars that have published phase-resolved spectra. This study indicated an increase of σ with the spin-down rate \dot{E} and a decrease with the pulsar age.

In Kalapotharakos et al. (2017), guided by *Fermi* observations, we expanded our studies and we refined the FIDO models by restricting the dissipative regions outside the LC only near the ECS. Running series of models that covered the entire range of the observed \dot{E} of Young Pulsars (YP) and Millisecond Pulsars (MP), and matching the corresponding cutoff energies ϵ_{cut} we revealed a dependence of σ with \dot{E} . We found that σ increases with \dot{E} for high \dot{E} while it saturates for low \dot{E} . We also found clear indications that the size of the dissipative zones increase towards low \dot{E} and that the multiplicity of the emitting particles increase with \dot{E} and α .

Recently, a new approach has been explored to model pulsar magnetospheres. A few groups attempted to build kinetic models of pulsar magnetospheres using the Particle-In-Cell (PIC) technique, when charged particle trajectories and electromagnetic fields are treated self-consistently (Philippov & Spitkovsky 2014; Chen & Beloborodov 2014; Cerutti et al. 2015; Philippov et al. 2015a; Philippov et al. 2015b; Belyaev 2015b,a; Cerutti et al. 2016; Brambilla et al. 2017). Some of these studies (Chen & Beloborodov 2014; Philippov et al. 2015a; Belyaev 2015a) tried to simulate the pair-creation physics but failed to produce magnetospheres of low inclination angles filled with plasma close to the FF ones. One of the problems in these studies is the poor numerical resolution inherent to any global model which might prevent an accurate modeling of microphysics of particle acceleration and pair production. Cerutti et al. (2016) studied

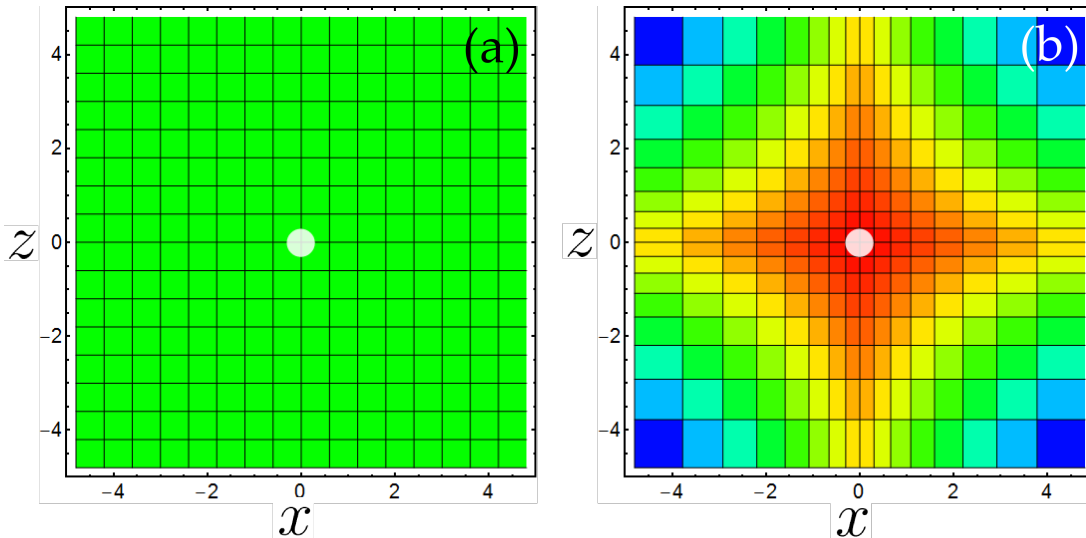


Figure 1. (a), (b) A 2D slice of the uniform and non-uniform distribution of the computational domain implemented in the C-3PA code. The structure shown in (b) takes care the load balance issue by taking into account the fact that the central regions have much higher particle number densities. Moreover, the implementation (b) keeps the original simple cartesian communication between the CPUs that “control” the various sub-domains (i.e. cuboids). Even though the implementation (b) is still not optimum it can reduce the total computational times, relatively to the implementation (a), by ~ 1 order of magnitude.

the high-energy emission from their PIC simulations and found that the main source is synchrotron radiation but with fixed (with $\dot{\mathcal{E}}$) γ -ray efficiency (not totally consistent with the observations; 2PC). More recently, [Philippov & Spitkovsky \(2017\)](#) agreed that higher particle multiplicities (i.e. higher σ) from pair creation in the outer magnetosphere is needed at higher $\dot{\mathcal{E}}$ values to explain the dependence of the total γ -ray luminosity on $\dot{\mathcal{E}}$ (i.e. $L_\gamma \propto \dot{\mathcal{E}}^{1/2}$).

In the present paper, we present our PIC code and we make the first step by applying ad-hoc (not physically motivated) particle injections which provide at least field configurations and particle distributions that are consistent with each other. The main goal of this study is to explore the role of the global particle injection rate \mathcal{F} in both the development of the field structures toward the FF regime and the characteristics of the corresponding high-energy emission. More specifically, taking into account the constraints imposed by *Fermi* data we reveal a relation between \mathcal{F} and $\dot{\mathcal{E}}$ that is able to reproduce a broad spectrum of the observed phenomenology (i.e. γ -ray light-curves and spectra).

The structure of the paper is as follows. In Section 2, we introduce our PIC code, discuss technical details, and present some basic tests. In Section 3, we discuss how we build our models and the adopted model parameters. In Section 4, we show a development of solutions from the VRD to the FF one as a function of the particle injection rate, \mathcal{F} . In Section 5, we discuss the model interpretation and the method we use in order to scale the particle energies as well as the corresponding emitted photon energies to those of real pulsars. In Section 6, we present our main results for two series of models that cover the observed $\dot{\mathcal{E}}$ -values of YPs and MPs. For these models, we show the dependence of the spectral cutoff energies with \mathcal{F} which, by taking into account the variation of the *Fermi* ϵ_{cut} , leads to a dependence of \mathcal{F} on $\dot{\mathcal{E}}$. Finally, in

Section 7, we summarize our conclusions and discuss the future prospects.

2. A PARTICLE-IN-CELL CODE: C-3PA

We have developed a **C**artesian **3D** **P**IC code for **A**strophysical studies (hereafter C-3PA). Our code follows the well known, simple but also powerful algorithm:

1. Integrate the time dependent Maxwell’s equations one time-step using the current provided by the particle collective motions.
2. Integrate the equations of motion one time-step for all the particles taking into account the field structure.
3. Goto 1.

Our code is written in Fortran 90 and is fully parallelized through Message Passing Interface (MPI). The code is charge conservative and in the current version it uses the so called cloud-in-cell (CIC) scheme for the shape function (i.e. the shape of each macroparticle is a cube of equal size with one grid cell of the lattice; see [Villasenor & Buneman 1992](#)). For the particle mover we implemented Vay’s algorithm ([Vay 2008](#)), which, in general, provides better accuracy for the drift motion of relativistic particle trajectories (compared to the standard Boris algorithm; see [Birdsall & Langdon 1991](#) and references therein). The forces exerted on the particles are weighted over the individual cubic particle shapes. The field solver integrates the time dependent Maxwell’s equations through a Finite-Difference-Time-Domain (FDTD) method applied in a Yee staggered mesh. In the outer boundary we use a Perfectly Matched Layer (PML; [Berenger 1996](#); [Kalapotharakos & Contopoulos 2009](#)) that absorbs the outgoing electromagnetic waves and minimizes the inward reflections. PML is applied outside a central cubic domain with side

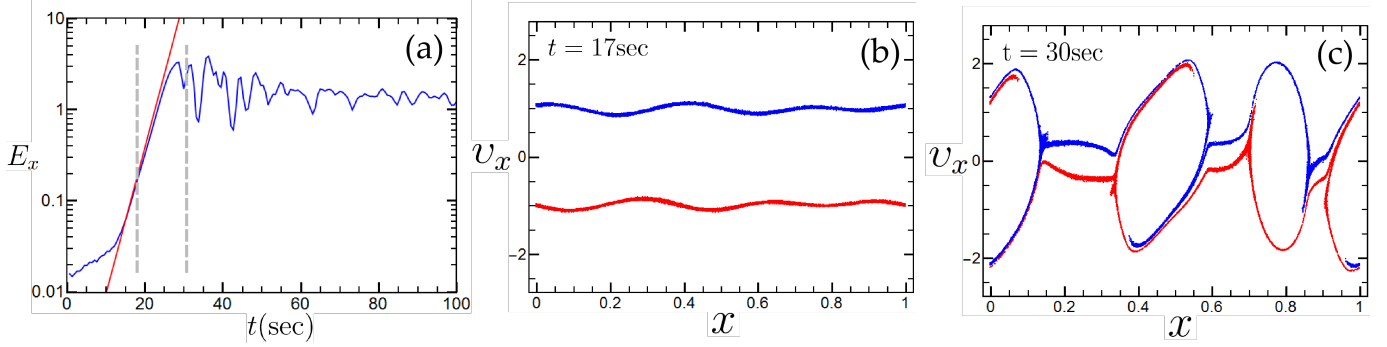


Figure 2. The two stream instability test for C-3PA code. In (a) the blue line shows the simulated maximum electric field component along the charge motion direction as a function of time. The red solid line indicates the theoretical growth rate. We see that the simulation behaves as theoretically expected. In (b) and (c) we plot the phase space portraits corresponding to the snapshots indicated by the vertical dashed gray lines in (a).

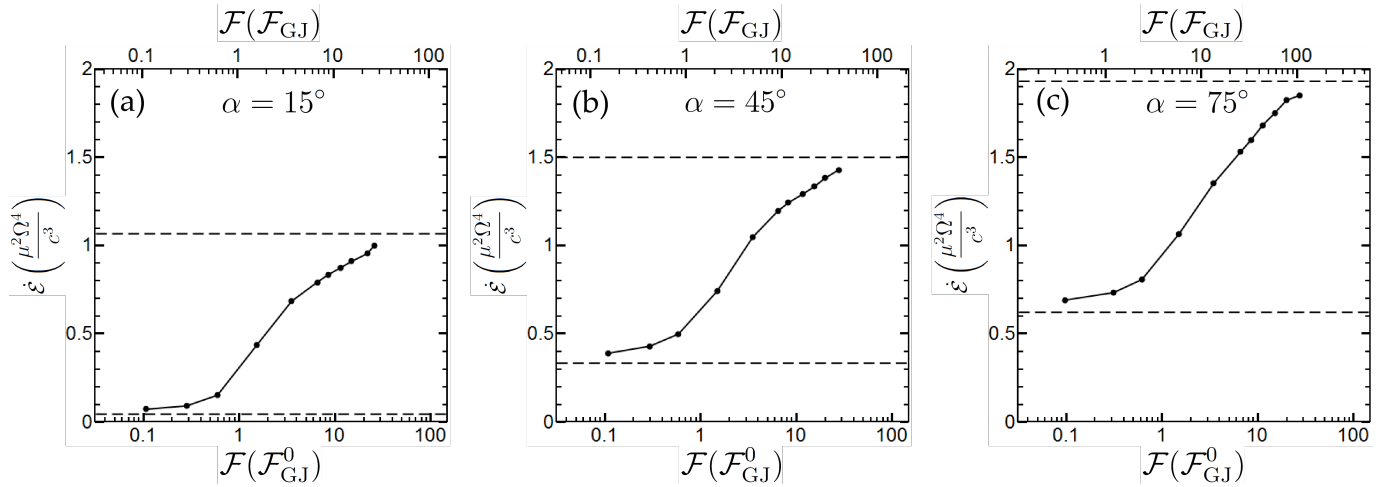


Figure 3. The spin-down power, for the indicated α values, as a function of the global particle injection rate, \mathcal{F} , in log-linear plots. On the bottom horizontal axis \mathcal{F} is presented in units of $\mathcal{F}_{\text{GJ}}^0$ (i.e. the particle injection rate that corresponds to the GJ flux from the two polar caps of the aligned, $\alpha = 0^\circ$, rotator) while on the top horizontal axis \mathcal{F} is presented in units of \mathcal{F}_{GJ} (i.e. the particle injection rate that corresponds to the GJ flux from the two polar caps of the corresponding α value). In each panel the two dashed horizontal lines indicate the VRD (lower) and FF (higher) $\dot{\mathcal{E}}$ values, respectively.

$\approx 8.6 R_{\text{LC}}$ (where R_{LC} is the light-cylinder radius) and its width is $\approx 0.5 R_{\text{LC}}$. The particles are removed from the simulation after they enter the outer layer. They are also removed when their entire shape enters the central spherical conductor (rotating NS). Moreover, a gaussian kernel can be applied for the current density that mimics a higher order shape function reducing considerably the noise level.

Inside the stellar surface the electric field is always defined by Eq. (1). The problem of this configuration is that it does not incorporate the current closure of the charge carriers that reach the stellar surface. This leads to the charging of the surface mostly in the regions the polar-cap passes through (see also Spitkovsky & Arons 2002). The problem is more prominent for low α -values because the corresponding polar-caps do not significantly change their position on the spherical surface. Philippov & Spitkovsky (2014) in order to resolve this problem, simulated the behavior of the spherical conductor by enforcing charge motions inside the conductor that restore/sustain the electric field of Eq. (1). Nonetheless, in our simulations, we have adopted a much simpler and

less computationally expensive method. Namely, we integrate Maxwell's equations down to the stellar radius while at the end of each time-step we enforce \mathbf{E} , within a thin layer (~ 3 cells wide) outside the stellar surface, to go to the conductive value (i.e. Eq. 1). This treatment “cleans” the traces of the charges that enter the stellar surface and it actually mimics the current that maintains the electric field in the conductor. In this approach, the outer surface of this thin layer determines the effective stellar surface.

We have also incorporated into the particle equations of motion the radiation reaction forces. The complete expression reads (Landau & Lifshitz 1987)

$$\begin{aligned} \mathbf{F}_{\text{rr}} = & \frac{2q_e^4}{3m_e^2 c^4} \left[\mathbf{E} \times \mathbf{B} + \mathbf{B} \times \left(\mathbf{B} \times \frac{\mathbf{v}}{c} \right) + \mathbf{E} \left(\frac{\mathbf{v}}{c} \cdot \mathbf{E} \right) \right] \\ & - \frac{2q_e^4 \gamma_L^2}{3m_e^2 c^5} \mathbf{v} \left[\left(\mathbf{E} + \frac{\mathbf{v}}{c} \times \mathbf{B} \right)^2 - \left(\mathbf{E} \cdot \frac{\mathbf{v}}{c} \right)^2 \right] \\ & + \frac{2q_e^4 \gamma_L}{3m_e c^3} \left[\left(\frac{\partial}{\partial t} + \mathbf{v} \cdot \nabla \right) \mathbf{E} + \frac{\mathbf{v}}{c} \times \left(\frac{\partial}{\partial t} + \mathbf{v} \cdot \nabla \right) \mathbf{B} \right] \end{aligned} \quad (2)$$

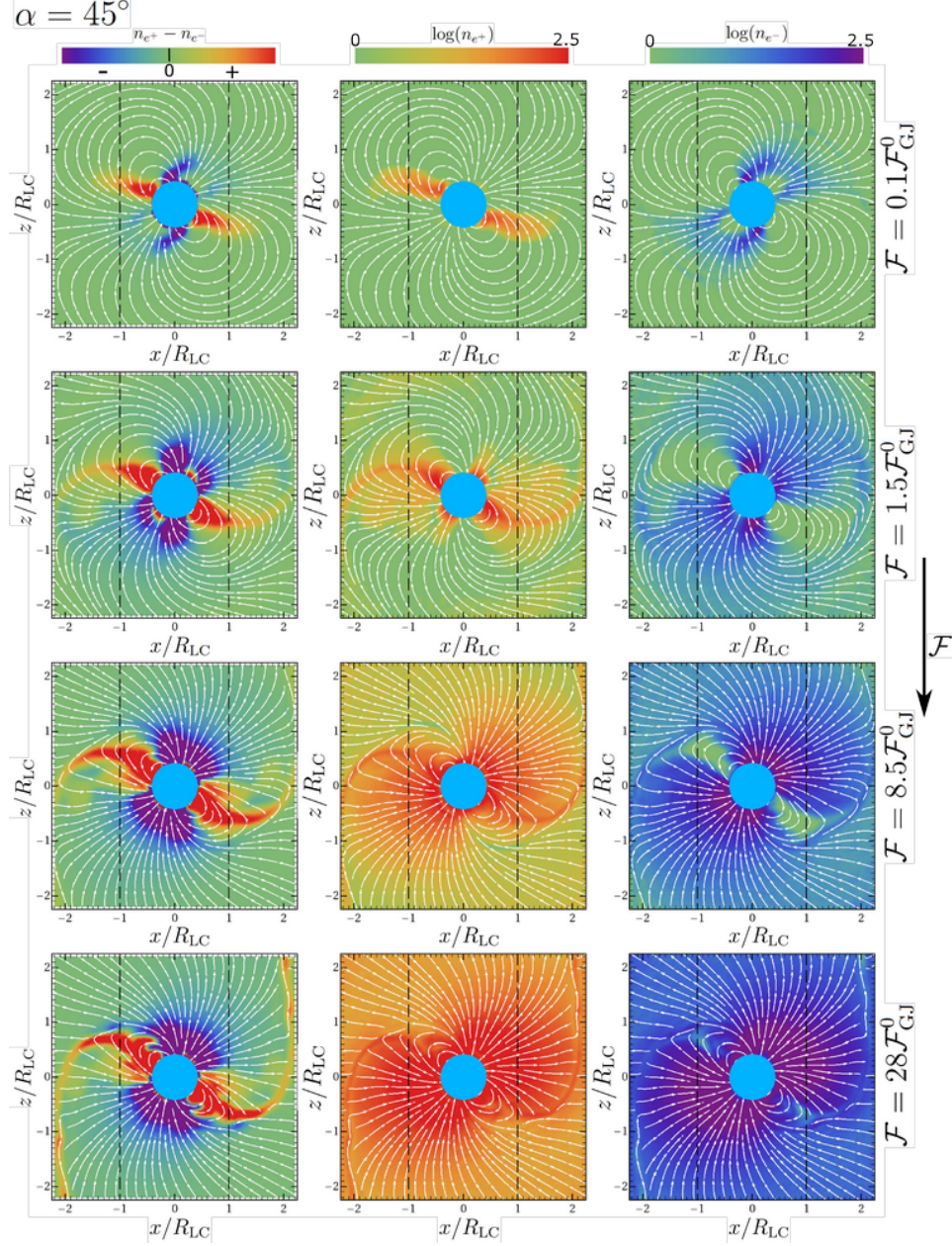


Figure 4. In the left-hand, middle, and right-hand columns we plot, on the $\mu - \Omega$ plane, the charge density, e^+ number density, and e^- number density, respectively, in the indicated color scales, for simulations of $\alpha = 45^\circ$. In each panel, the white lines show the poloidal magnetic field while each row corresponds to simulations for the \mathcal{F} values indicated in the figure. The vertical black lines indicate the LC.

where q_e , m_e are the electron charge and mass, respectively and \mathbf{v} , γ_L are the corresponding particle velocity and Lorentz factor. The third term involves the convective derivatives of the fields and besides the implementation difficulty especially in an evolving system we have found (by applying it to stationary magnetosphere solutions) that it is negligible compared to the first two terms (see also Cerutti et al. 2016; Tamburini et al. 2010). Thus, in C-3PA we have incorporated only the first two terms following the numerical scheme suggested in Tamburini et al. (2010).

In almost every PIC code the run time is determined

mainly by the work load that corresponds to the integration of the particle equations of motion (and not the integration of Maxwell's equations). In our problem the spatial particle distribution is quite non-uniform. The particle number density outside the stellar surface is much higher than the one at the edges of the computational domain. Assuming an MPI implementation where all the central processing units (CPUs) “control” equal computational volumes (Fig. 1a) the performance is slower (in several cases by more than one order of magnitude) compared to the theoretical one that corresponds to the total number of operating CPUs. This happens because the CPUs that “control” the outer parts of the domain have to wait for the inner CPUs to finish the

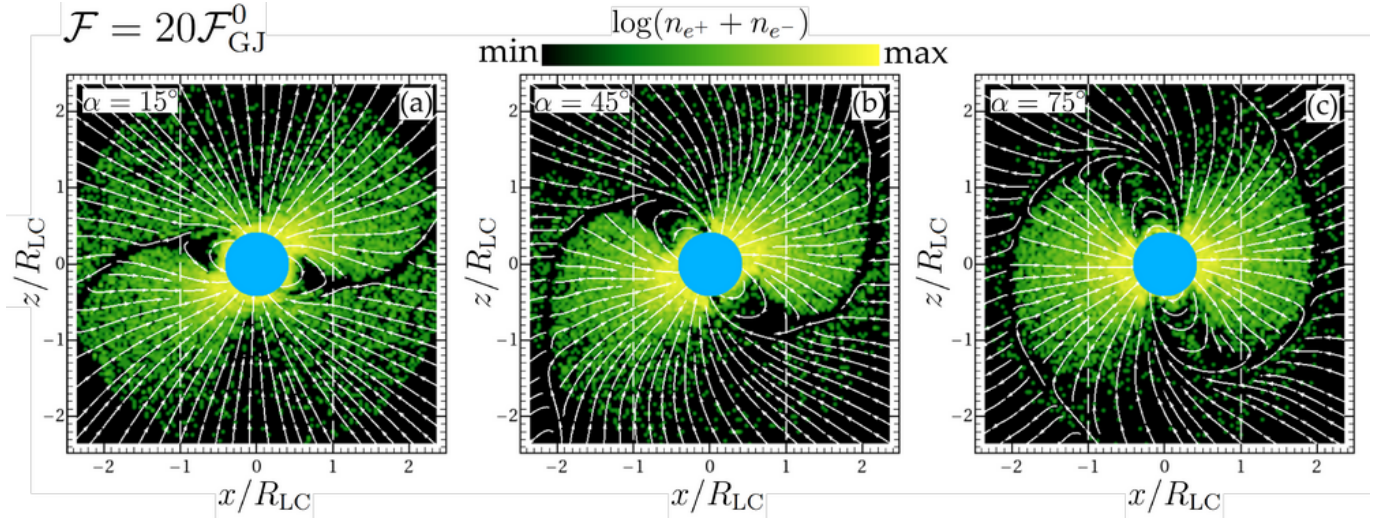


Figure 5. The number density of the particles that are injected per time-unit, in the indicated logarithmic color scale. The plotted results are on the $\mu - \Omega$ plane for the indicated α values and for $\mathcal{F} = 20\mathcal{F}_{\text{GJ}}^0$. The solid white lines indicate the poloidal magnetic field lines while the vertical dashed white lines point out the LC.

	$\alpha = 15^\circ$	$\alpha = 45^\circ$	$\alpha = 75^\circ$
$\mathcal{F}(\mathcal{F}_{\text{GJ}}^0)$	$\mathcal{F}(\mathcal{F}_{\text{GJ}})$	$\mathcal{F}(\mathcal{F}_{\text{GJ}})$	$\mathcal{F}(\mathcal{F}_{\text{GJ}})$
0.1	0.1	0.14	0.38
0.25	0.26	0.35	0.97
0.6	0.62	0.85	2.3
1.5	1.55	2.1	5.8
3.5	3.6	4.9	13.5
6.5	6.7	9.2	25.1
8.5	8.8	12.0	32.8
11.5	11.9	16.2	44.4
15.0	15.5	21.2	58.0
20.0	20.7	28.3	77.3
28.0	29.0	39.6	108.2

Table 1

We present models corresponding to 11 \mathcal{F} values. In the first column, the adopted \mathcal{F} values are shown in the $\mathcal{F}_{\text{GJ}}^0$ unit (i.e. the particle injection rate that corresponds to the GJ flux from the two polar caps of the aligned, $\alpha = 0^\circ$, rotator). The second to fourth columns show the adopted \mathcal{F} values in \mathcal{F}_{GJ} units (i.e. the particle injection rate that corresponds to the GJ flux from the two polar caps for the indicated α value).

calculations for relatively much higher numbers of particles. C-3PA takes care of this load balance issue by implementing a rather simple non-uniform volume distribution (Fig. 1b) that, in general, increases the controlled volume with the distance from the center. The advantage of the scheme shown in Fig. 1b is that it keeps a straight-forward communication between the neighbor cuboids. A proper choice of the different length sizes of the rectangular cuboids (rectangles in Fig. 1b) improves considerably the computational speed. In particular, for simulations with $16^3 = 4096$ CPUs, we gain a factor ~ 7 .

Besides all trivial tests, we have reproduced the two stream instability (Birdsall & Langdon 1991). It is well known that two sets of opposite streams of charged particles is unstable. Any small charge imbalance (i.e. perturbation) creates an electric field along the motion direction that grows exponentially. In Fig. 2a we show, for a configuration of initially two opposite streams of e^- within a proton background, the evolution of the maximum electric field E_x along the motion direction x . The blue line corresponds to the simulated data while the red

line indicates the theoretical growth rate which is equal to $\omega_p/2$ where ω_p is the electron plasma frequency. Figure 2b,c show the phase space for the indicated times (see also the dashed light gray vertical lines in Fig. 2a) that correspond to a snapshot during the exponential growth and to a snapshot when the instability has been fully developed.

3. SIMULATION SETUP

The present study focuses on exploring self-consistent pulsar magnetosphere models that neglect the pair creation microphysics. As mentioned above, the primary goal is to find how the solutions and the related properties depend on a single parameter, the global particle injection rate \mathcal{F} . Thus, for the models presented throughout this paper the particle injection is made based on the following prescription: at each time-step and at each cell up to $r = 2.5R_{\text{LC}}$ one pair (e^+ , e^-) is injected at rest ($\gamma_L = 1$; γ_L is the Lorentz factor) as long as the plasma magnetization

$$\sigma_M = \frac{B^2}{8\pi(n_{e^+} + n_{e^-})m_e c^2} \quad (3)$$

exceeds a locally predefined value, Σ , that varies according to

$$\Sigma = \begin{cases} \Sigma_0 \left(\frac{r_s}{r}\right)^3 & \text{if } r \leq R_{\text{LC}} \\ \Sigma_0 \left(\frac{r_s}{R_{\text{LC}}}\right)^3 \frac{R_{\text{LC}}}{r} & \text{if } r > R_{\text{LC}} \end{cases} \quad (4)$$

where m_e is the electron mass, n_{e^-} and n_{e^+} are the e^- and e^+ number densities, r_s is the stellar radius in the simulation, and Σ_0 is the value of Σ at $r = r_s$. Our code starts with some initial (estimated) Σ_0 value which is adjusted in time so that \mathcal{F} reaches the originally adopted goal-value. The \mathcal{F} unit corresponds to the Goldreich-Julian flux from both polar-caps $\mathcal{F}_{\text{GJ}} = \mathcal{F}_{\text{GJ}}^0 \cos(\alpha)$ ¹,

¹ This definition breaks down very close to $\alpha = 90^\circ$ where a more detailed calculation is needed that takes into account the particle

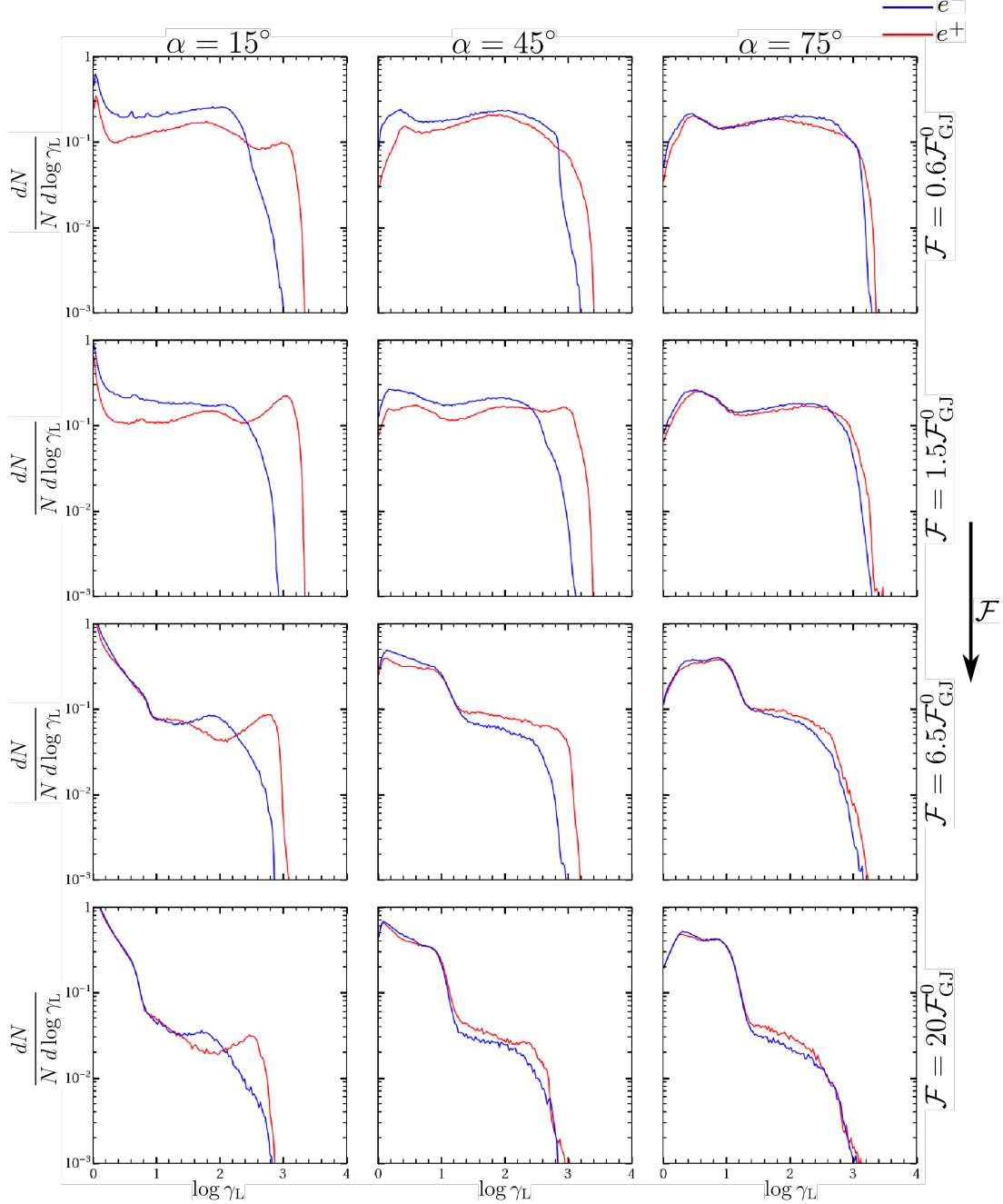


Figure 6. The normalized e^- (blue) and e^+ (red) energy distributions. Each column corresponds to the indicated α values while each row corresponds to the indicated \mathcal{F} values.

where $\mathcal{F}_{\text{GJ}}^0 = B_s \Omega A_{\text{pc}} / (\pi q_e)$ (q_e is the elementary electric charge, B_s is the stellar surface magnetic field, and A_{pc} is the corresponding polar cap area) is the \mathcal{F}_{GJ} value for $\alpha = 0^\circ$.

Starting from a configuration close to the VRD, we start injecting particles based on the aforementioned prescription and let our simulations evolve for at least 1.5 periods while the steady-state is achieved after ~ 1 period.

The stellar period in the simulation is $P_s = 0.1\text{s}$ which

number density (n_{GJ}) distribution on the entire polar cap and not only the value at the magnetic pole.

places the LC at $R_{\text{LC}} = 4.8 \times 10^8 \text{cm}$. The adopted magnetic field at $r_* = 10 \text{km}$ (actual NS radius) is $B_s = 10^6 \text{G}$ which allows us to achieve high magnetization values even for the highest injection rates. For the simulations with the highest particle injection rates the magnetization is ~ 500 at the stellar surface and ~ 40 near the LC and it never falls below 10 in the regions² we present our results. We have also run simulations with $B_s = 10^5 \text{G}$ and the results presented below remained unaffected. If not mentioned otherwise the simulation resolution pre-

² The regions near the ECS where the local B value decreases dramatically are excluded.

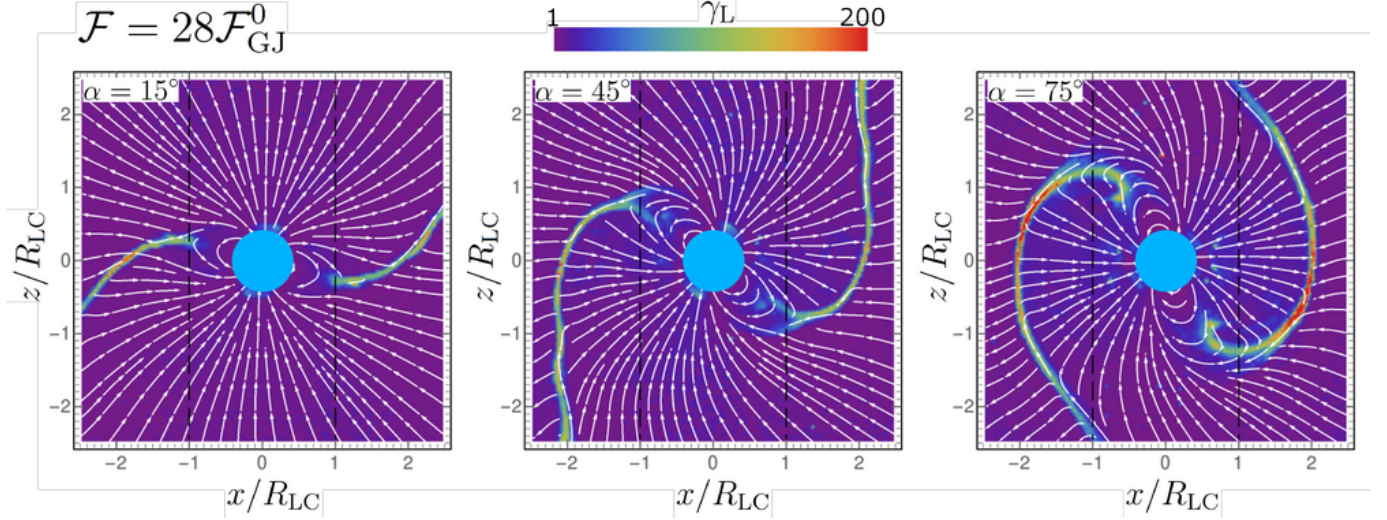


Figure 7. The average (per computational cell) γ_L values in the indicated color scale. The plots are for $\mathcal{F} = 28\mathcal{F}_{GJ}^0$ while each panel corresponds to the indicated α value. The high-energy particles lie near the ECS outside the LC (black dashed vertical lines).

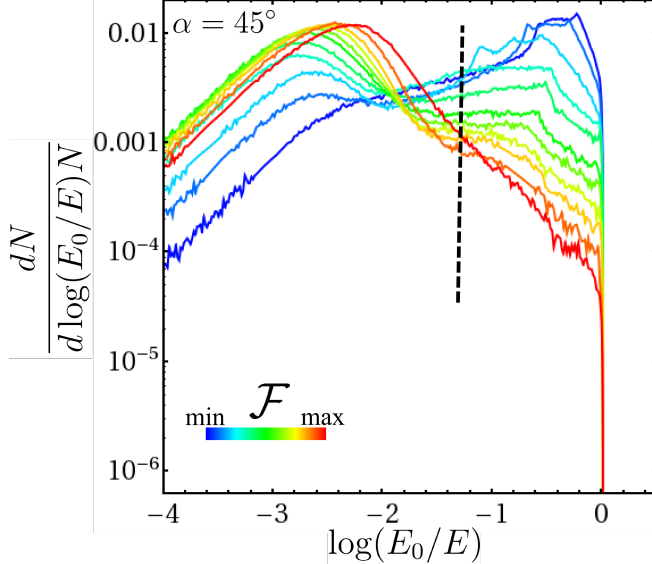


Figure 8. The distribution, in log-log scale, of the E_0/E values calculated at points randomly selected within the spherical shell that is defined by the stellar surface and the sphere with $r = 2.0$. The point density corresponds to ~ 1 point per computational cell. The plotted results correspond to simulations of $\alpha = 45^\circ$. The different colors correspond to different \mathcal{F} values. As shown in the Figure \mathcal{F} increases as the color changes gradually from blue to red. The vertical dashed line makes the value to the right of which we consider that the actual acceleration takes place.

sented below is 25 grid points per R_{LC} . The simulating stellar radius is at $r_s = 0.28R_{LC}$ (resolved by 7 grid points) while the kernel layer thickness is 2.5 grid cells which places the effective stellar radius at $r_{eff} = 0.38R_{LC}$.

The charge q_M of the individual macroparticles determines, for each \mathcal{F} -value, the average number N_{Mc} of macroparticles per cell. The smaller the q_M (i.e. higher N_{Mc}) the lower the noise level (i.e. the field and current fluctuations). However, we have found that the higher the \mathcal{F} the lower the q_M should be in order to keep the noise at relatively low levels. As we also discuss in Sec-

tion 5 for solutions near the FF (i.e. high \mathcal{F}) the actual accelerating electric fields become small and the noisy fields can become comparable. Apparently, this implies that for higher \mathcal{F} we need disproportionately high numbers of macroparticles which makes the corresponding simulations very expensive.

The time-step $\Delta t_s = 4 \times 10^{-5} P_s$ guarantees that, for the most dense magnetosphere regions of the models with the highest injections rates presented in this paper, $(\omega_p \Delta t_s)^{-1} > 6$, where ω_p is the fundamental plasma frequency $\omega_p = \sqrt{4\pi(n_{e+} + n_{e-})q_e^2/m_e}$. In some cases the adopted global time-step doesn't resolve the gyro-motion. In these cases, the particle equations of motion are integrated by smaller time-steps. Following the orbits finely doesn't affect the currents that depend only on the motion within the global time-step. Nonetheless, we have found that it provides more accurate particle energies and as we discuss in Section 5 allows us to adjust the particle gyro-motion.

We note that in some cases, the adopted regular spatial resolution does not resolve the skin-depth $\lambda_D = c/\omega_p$ for the low γ_L particles in the most dense magnetosphere regions. This implies that this particle population could be artificially heated to energies higher than expected physically. However, the corresponding thermal γ_L values are much smaller (~ 1 order of magnitude) than that corresponding to the full potential drop across the polar-cap (i.e. $\gamma_{Lmax} = q_e B_s r_*^3 / m_e c^2 R_{LC}^2$) while the number of these particles seems to be small and doesn't affect the particle energy distributions. Actually, we have found that the particle energy distribution is more sensitive to the q_M and Δt_s values discussed above. Nonetheless, we have run simulations for the highest \mathcal{F} -values doubling the spatial resolution, and the particle energy distributions and all the results presented in the next sections remained unaffected.

4. TOWARDS THE FF SOLUTIONS

We present simulations for $\alpha = 15^\circ$, $\alpha = 45^\circ$, and $\alpha = 75^\circ$. For each of these α -values, we have simulated 11 \mathcal{F} -values that effectively produce an entire spectrum of

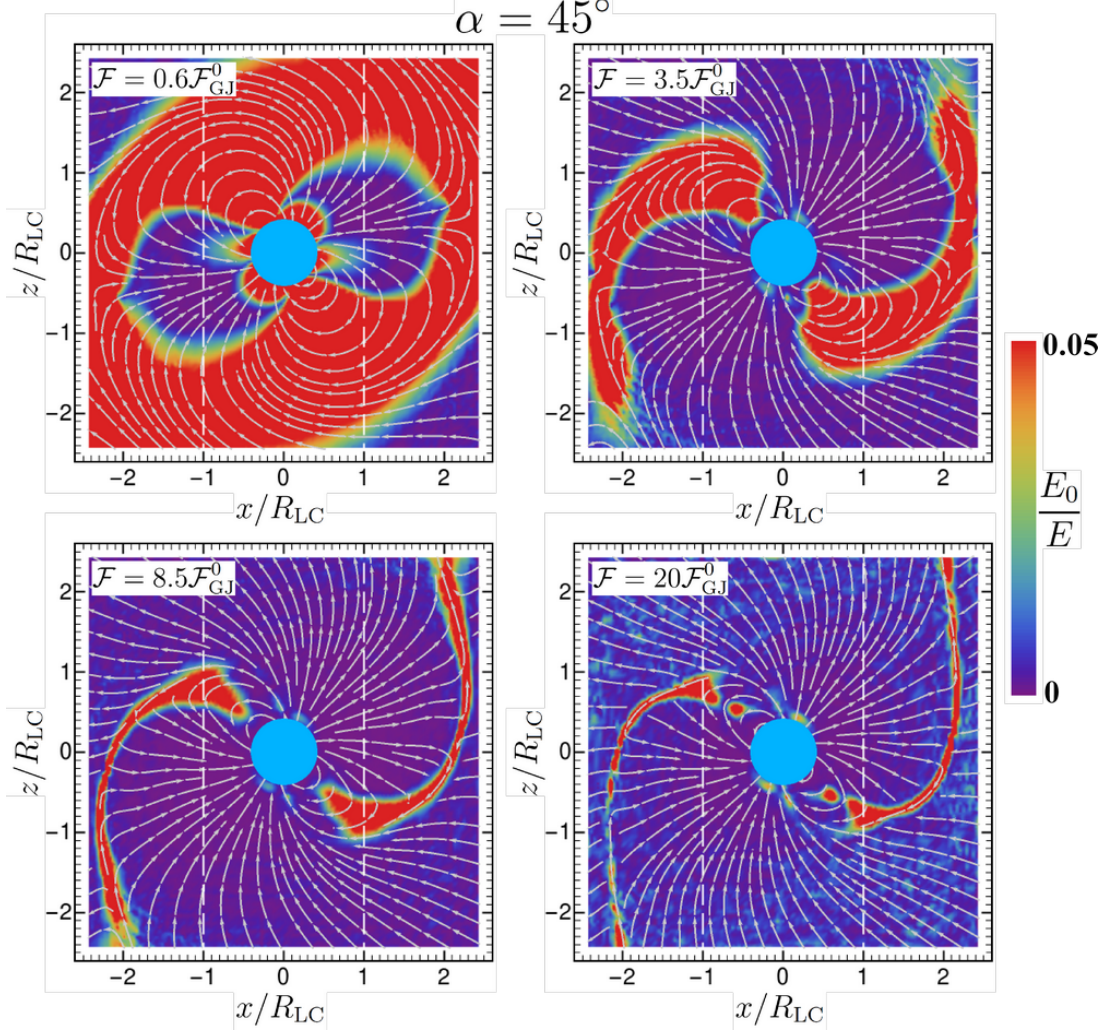


Figure 9. The spatial distribution of E_0/E , in the indicated color scale, for simulations of $\alpha = 45^\circ$. Each panel corresponds to the indicated \mathcal{F} values. The red colored regions correspond to the regions above the value indicated by the vertical dashed line in Fig. 8.

solutions from close to VRD to close to FF. Table 1 shows the adopted \mathcal{F} values in $\mathcal{F}_{\text{GJ}}^0$ units (second column) and in the corresponding \mathcal{F}_{GJ} units (third to fifth column).

Figure 3 presents, for the indicated α -values, the spin-down power, $\dot{\mathcal{E}}$ vs. particle injection rate, \mathcal{F} in a log-linear plot. We see that for low and high \mathcal{F} -values $\dot{\mathcal{E}}$ asymptotically goes to the values corresponding to VRD and FF ones denoted by the dashed lines.

In Fig. 4, we see the field structure, for $\alpha = 45^\circ$ and for the indicated \mathcal{F} -values, on the poloidal $\mu - \Omega$ plane. The charge density ρ (left-hand column) as well as the number density of positrons n_{e^+} (middle column) and electrons n_{e^-} (right-hand column) are shown in the indicated color scales. As \mathcal{F} increases features of the FF solution start developing. Thus, the magnetic field lines open gradually beyond the LC and become straight, while the ECS beyond the LC starts forming. The low \mathcal{F} magnetospheres (i.e. top row) tend to be charge-separated (similar to the dome-torus configuration; see Krause-Polstorff & Michel 1985; Spitkovsky & Arons 2002) while the high \mathcal{F} -values produce magnetospheres with both kinds of charge carriers being abundant everywhere (i.e. bottom row).

Figure 5 shows, in a logarithmic scale on the $\mu - \Omega$

plane, the number density of the injected particles per unit time for the indicated α -values and for a high injection rate ($\mathcal{F} = 20\mathcal{F}_{\text{GJ}}^0$). The much higher densities near the stellar surface are compensated by the much larger volumes at larger distances. We note that our injection prescription activates particles injection only when magnetization σ_{M} exceeds some threshold value (Eq. 4) and so particle injection is strongly suppressed in the ECS region outside the LC where $B \rightarrow 0$. This implies that in our simulations the particles appearing eventually in the ECS originate from the separatrix within the LC and/or reach the ECS region by drifting across magnetic field lines (see also the discussion in Section 6). In Brambilla et al. (2017), studying magnetospheres with particles injected only near the stellar surface, we saw drifting positrons contributing to the structure of the ECS.

Figure 6 shows for the indicated α , \mathcal{F} values the normalized particle energy (i.e. γ_L) distributions for both e^- (blue lines) and e^+ (red lines). These distributions consist of a low energy population that peaks at $\gamma_L \sim 1$ and one at higher energy ($\gamma_L \gtrsim 30$) that extends to $\gamma_L \sim 10^3$. The first component is the non-accelerated bulk plasma, which is associated mainly with the short scale ($\sim \lambda_D$)

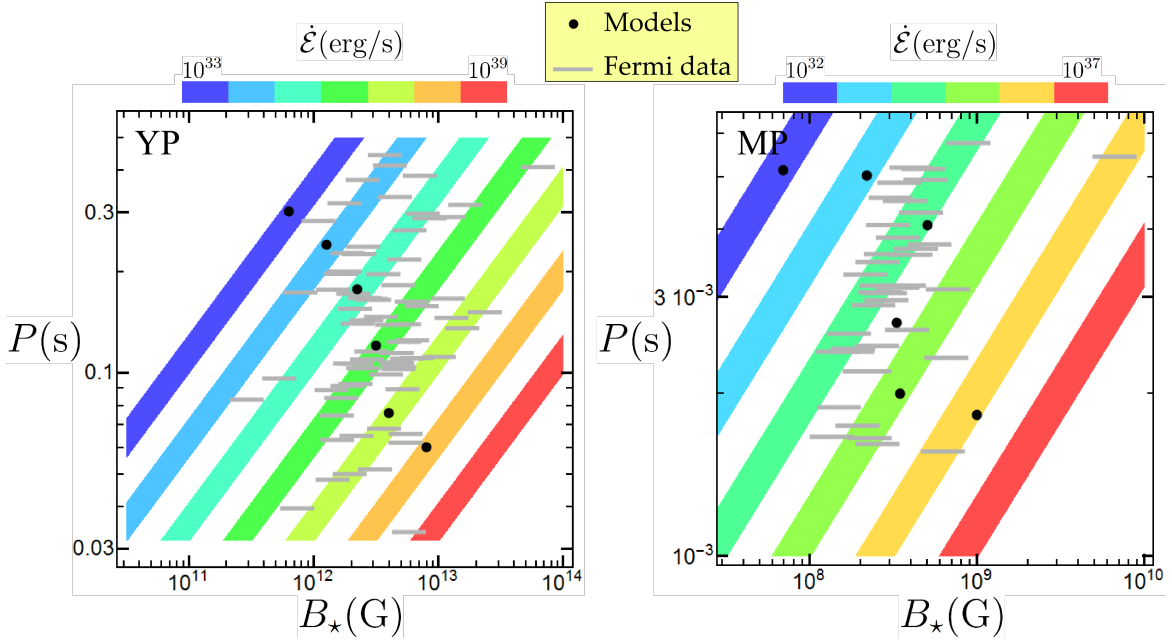


Figure 10. The B_* vs. P values of the *Fermi* pulsars together with the adopted realistic model values (see Table 2). The left and right hand panels correspond to YPs and MPs, respectively. The large black dots denote the model points while the gray horizontal segments denote the *Fermi* data. The width of these segments indicate the B_* uncertainty. More specifically, the left and right edges of these segments correspond to the B_* value assuming the spin-down power of the perpendicular rotator ($\alpha = 90^\circ$) for the VRD and FF regimes, respectively. The colored stripes denote the indicated $\dot{\mathcal{E}}$ values with the B_* uncertainty discussed above. We see that the 12 model points trace well the “observed” area of the diagrams.

Model No.	Young Pulsars			Millisecond Pulsars		
	B_* (10^{12} G)	P (ms)	$\dot{\mathcal{E}}_{\text{FF}}$ (erg s^{-1})	B_* (10^8 G)	P (ms)	$\dot{\mathcal{E}}_{\text{FF}}$ (erg s^{-1})
1	0.63	302.0	$(0.5 - 1.4) \times 10^{33}$	0.7	5.1	$(0.7 - 2.0) \times 10^{32}$
2	1.26	239.9	$(0.5 - 1.4) \times 10^{34}$	2.2	5.0	$(0.7 - 2.2) \times 10^{33}$
3	2.24	177.8	$(0.5 - 1.4) \times 10^{35}$	5.0	4.1	$(0.9 - 2.6) \times 10^{34}$
4	3.16	398.1	$(0.5 - 1.4) \times 10^{36}$	3.3	2.7	$(2.0 - 6.0) \times 10^{34}$
5	3.98	223.9	$(0.5 - 1.4) \times 10^{37}$	3.5	2.0	$(0.7 - 2.2) \times 10^{35}$
6	7.94	125.9	$(0.5 - 1.4) \times 10^{38}$	10.0	1.8	$(0.9 - 2.6) \times 10^{36}$

Table 2

The 12 (6+6) adopted realistic (B_* , P) value sets for YP and MP models. For each value set the FF spin-down power range is indicated (see Eq. 10b).

fluctuating fields while the second component is the accelerating component, which is associated with the larger scale unscreened fields of the magnetosphere. We note that the relative strength of the accelerating component decreases with increasing \mathcal{F} . As we also discuss later a significant part of the particle acceleration takes place at large distances at and beyond the LC, even for relatively low \mathcal{F} (i.e. $\mathcal{F} \gtrsim 1\mathcal{F}_{\text{GJ}}^0$). However, for high \mathcal{F} values and solutions close to the FF ones the acceleration takes place exclusively at and beyond the LC in regions near the ECS.

In Fig. 7 we plot, for different α -values and for $\mathcal{F} = 28\mathcal{F}_{\text{GJ}}^0$, the average (within a computational cell) γ_{L} -value. These simulations have field structures very close to the FF ones and the average γ_{L} -values indicate the existence of energetic particles only in the region close to the Y-point³ and the ECS beyond the LC. The FF ECS for $\alpha = 0^\circ$ is positively charged (i.e. $\rho > 0$) but as α increases the corresponding charge density decreases and

it becomes 0 for $\alpha = 90^\circ$ ⁴. This can be concluded also by the fact that the orthogonal rotator $\alpha = 90^\circ$ actually lies in the middle of the aligned and anti-aligned rotator. In Fig. 6 the consistent excess of positrons at high energies reflects the strong acceleration that takes place at and beyond the LC near the ECS⁵. The effect is suppressed as we go towards higher α -values.

5. INTERPRETING THE SIMULATIONS

In the previous section, we saw that an entire spectrum of solutions from near VRD to near FF ones can be covered by applying arbitrary particle injection everywhere in the magnetosphere. However, a vital question that arises is whether and how these simulations can be compared to the recent rich observational data

⁴ At $\alpha = 90^\circ$ the ECS consists of the same number of e^+ and e^- .

⁵ For low \mathcal{F} values, the notion of the ECS is not unambiguous. However, even in these cases the high accelerating electric components appear mainly in the regions that e^+ dominate and eventually (for high \mathcal{F} values) will form the ECS.

³ The point where the separatrix meets the ECS.

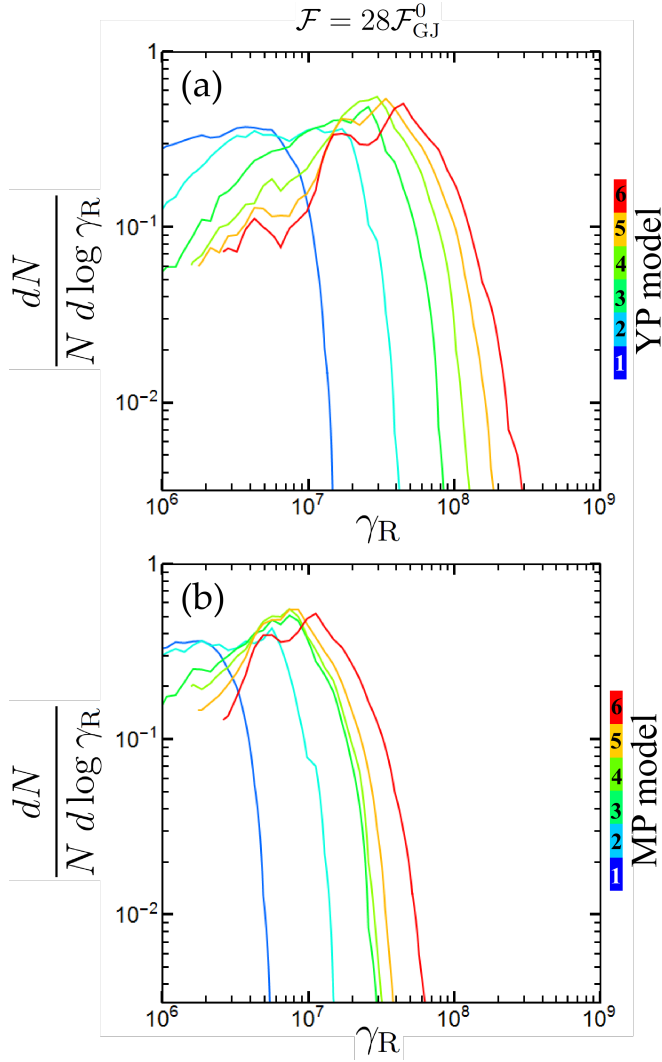


Figure 11. The distributions of the γ_R (see Eq. 8) values for $\mathcal{F} = 28\mathcal{F}_{\text{GJ}}^0$ and $\alpha = 45^\circ$. The top and the bottom panels show the results for YP and MP models. In each panel the different colors denote the indicated model No. (i.e. the different realistic B_* , P parameter values; see Table 2).

(i.e. *Fermi*). The comparison with the observations requires a detailed modeling of the high-energy emission in PIC simulations. This implies not only the determination of the emitting regions but also the derivation of the corresponding ϵ_{cut} and L_γ values. However, the PIC particle energies are much smaller than the energies in a real pulsar magnetosphere (see Fig. 6) due to the much smaller fields (see Section 3). In addition, there is no trivial relation (e.g. proportionality) that can provide the particle energy transformation between the PIC model and the real system. The PIC particles energies are not only smaller but are also crucially affected by the radiation reaction forces with the phenomenon being more prominent for the high-energy emitting particles. In our PIC simulations, the impact of the actual radiation reaction forces (Eq. 2) on the particles energies is small (due to the corresponding small γ_L and B values). Moreover, synchrotron and curvature losses act very differently depending strongly on the specific regime

(i.e. γ_L , B , radius of curvature R_C of the guiding center). Furthermore, the gyro-radius in PIC simulations is much larger than in real pulsar magnetospheres (in R_{LC} units) and in low field regions this can, in principle, affect magnetosphere features (see Cerutti et al. 2015).

In real pulsar magnetospheres particles will lose their perpendicular (to the magnetic field) momentum and therefore their pitch angle very fast due to the corresponding synchrotron losses (unless there is some mechanism to sustain pitch angles). Under this regime, particles remain at the zero Landau level thus terminating the synchrotron radiation emission. Nonetheless, there are, in principle, certain conditions that can sustain the pitch angles and make synchrotron emission important. Lyubarskii & Petrova (1998) showed that cyclotron resonant absorption of low energy radio photons is efficient in pulsar magnetosphere environments. In the regions (at high altitudes within the LC though) where the resonant condition is fulfilled, the Landau states are populated and the pitch angles of the particles increase up to the equilibrium point where the absorption energy gain balances the energy losses due to (mainly) synchrotron emission. In Harding & Kalapotharakos (2015) (see also Harding et al. 2008), we showed that this processes, in some cases (e.g. Crab pulsar) may be important for explaining the optical to hard X-ray observed emission. Moreover, Uzdensky & Spitkovsky (2014) showed that in the reconnection region at the ECS of a Crab-like pulsar equipartition can trigger synchrotron emission. Nonetheless, any synchrotron emission that is triggered by cyclotron resonant absorption of low energy radio photons contributes to energies much smaller than the cutoff energies observed by *Fermi* while the microphysical emission properties of the reconnection at the ECS is difficult to be studied properly in global magnetosphere simulations that resolve rather poorly the corresponding region.

Taking into account all the above, our approach, in the current study, is based on the assumption that the contribution of the synchrotron emission is small (especially in the *Fermi* energy band) because of the rapid decrease of the perpendicular (to B) momentum. Thus, we have chosen to artificially decrease the synchrotron cooling time in the PIC simulation by increasing properly the magnetic field B_{eff} that enters the radiation reaction forces (Eq. 2). The field value B_{eff} varies in time (for each particle trajectory) ensuring always that the corresponding synchrotron cooling time

$$t_{\text{sc}} = -\frac{\gamma}{\dot{\gamma}} \propto B_{\text{eff}}^{-2} \gamma_L^{-1} \quad (5)$$

is effectively small, which means much smaller than the light crossing time $t_l = 1/\Omega$ but always resolved by the adopted time-step (at least 5 times). This process provides particle trajectories that have geometric properties closer to the real ones but still the resulting particle energies are slightly different than the original ones and always much less than the particle energies in a real pulsar magnetosphere. In order to derive PIC particle energies of meaningful values, we scale up the particle energies to the values they would have for real pulsar surface fields assuming that the trajectories of the high-energy particle are geometrically correct. We have actually checked that the vast majority of the PIC high-energy particles have velocities very close to those predicted by the Aristotelian

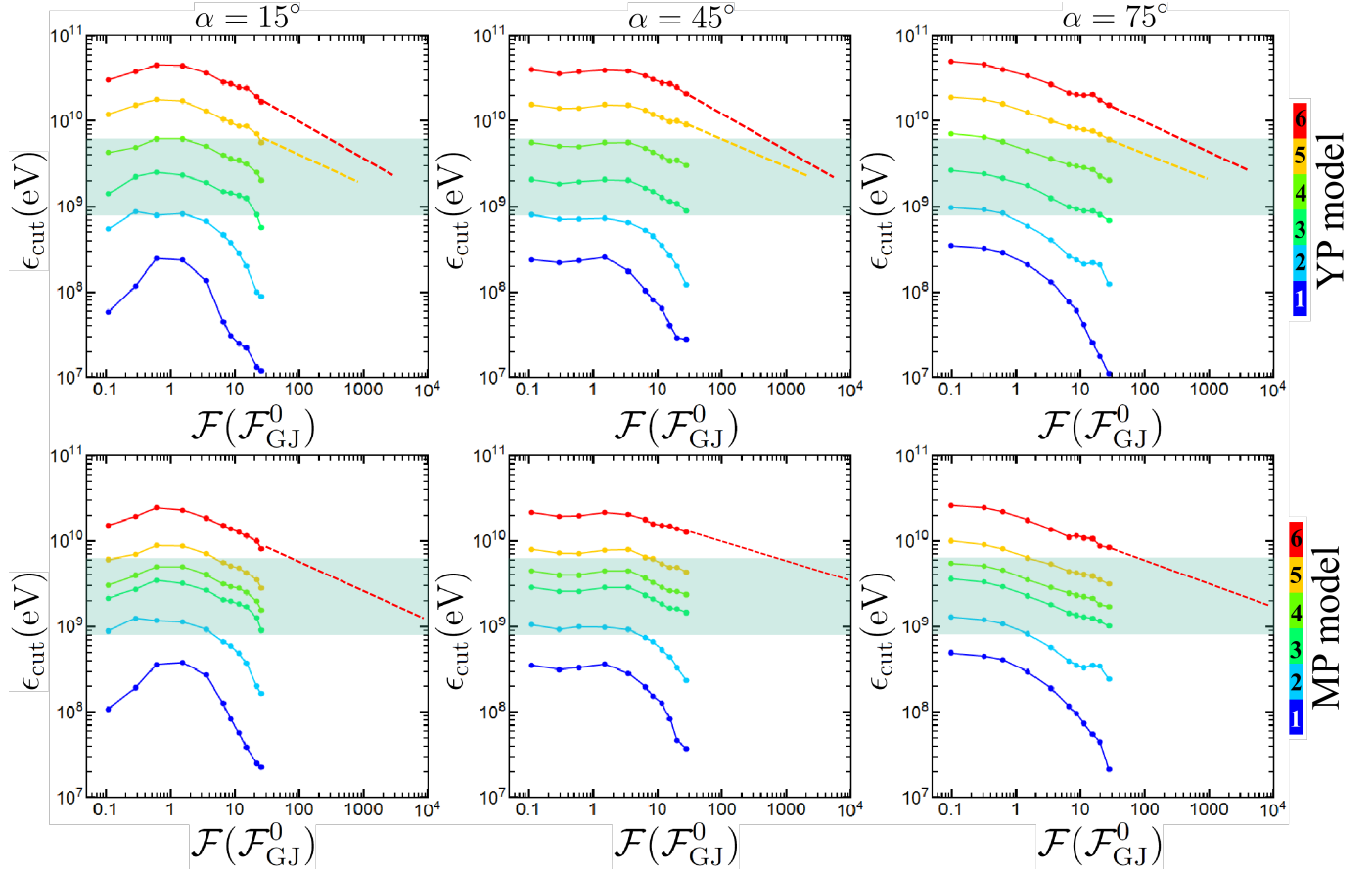


Figure 12. The ϵ_{cut} values of the model spectra as a function of \mathcal{F} in log-log scale diagrams. **Left-hand, middle, and right-hand** columns show the results for $\alpha = 15^\circ$, $\alpha = 45^\circ$, and $\alpha = 75^\circ$, respectively. The **top** and **bottom** rows show the results for YP and MP models, respectively. In each panel the different colors denote the indicated model No. (i.e. the different realistic B_* , P parameter values; see Table 2). The light greenish zones denote the zone of the observed (by *Fermi*) ϵ_{cut} values ($\sim 1 - 6$ GeV). The dashed lines are extrapolations that provide estimations of the \mathcal{F} values that produce ϵ_{cut} values within the *Fermi* (i.e. greenish) zone.

Electrodynamics (hereafter AE) (Gruzinov 2012)

$$\mathbf{v} = \frac{\mathbf{E} \times \mathbf{B} \pm (B_0 \mathbf{B} + E_0 \mathbf{E})}{B^2 + E_0^2} \quad (6)$$

which describes accurately the asymptotic behavior of the particle velocities. The two signs correspond to the two different types of charge while the quantities E_0 and B_0 are related to the Lorentz invariants (Gruzinov 2008; Li et al. 2012)

$$E_0 B_0 = \mathbf{E} \cdot \mathbf{B}, \quad E_0^2 - B_0^2 = E^2 - B^2 \quad (7)$$

and E_0 is the electric field in the frame where \mathbf{E} and \mathbf{B} are parallel and is the effective accelerating electric component E_{acc} which becomes zero only when $\mathbf{E} \cdot \mathbf{B} = 0$ and $E < B$. For the rest of the paper, E_0 denotes E_{acc} .

For the calculation of the scaled-up (i.e. realistic) particle energies, γ_R , we choose realistic P , B_* -values and we integrate along each particle trajectory the expression

$$\frac{d\gamma_R}{dt} = \frac{q_e \mathbf{v} \cdot \mathbf{E}}{m_e c^2} - \frac{2q_e^2 \gamma_R^4}{3R_C^2 m_e c} \quad (8)$$

which provides realistic γ_R values. We note that in Eq.(8), R_C is the local radius of curvature of the trajectory while \mathbf{v} is the corresponding particle velocity. Thus, the first and second terms in Eq.(8) denote the energy

gain (due to any accelerating electric field) and the energy losses due to CR reaction losses, respectively. For the calculation of R_C , 3 trajectory points are used that are separated in time d/c where d is the computational cell size. This implies that the R_C value is updated at intervals of d/c ⁶. Moreover, for the integration of Eq. (8), we take into account only the effective accelerating electric field components, as described below.

In our PIC simulations there are magnetosphere regions where nearly all the corresponding accelerating electric components are screened and magnetosphere regions with consistent accelerating electric components. The former regions are the effective FF regions where the field fluctuations dominate while the latter regions are the actual accelerating locations. We have found that the best way to identify these regions is to use the local values of the normalized effective accelerating electric field E_0/E , where E is the local total electric field. In Fig. 8, we plot, in log – log scale, the distributions of E_0/E values that have been calculated at points that are uniformly distributed within the magnetosphere volume that extends from the stellar surface up to $r = 2.5R_{\text{LC}}$. These results are for simulations with $\alpha = 45^\circ$ corre-

⁶ We have also checked different intervals (i.e. a few times d/c) for the update of R_C and our results remained unaffected.

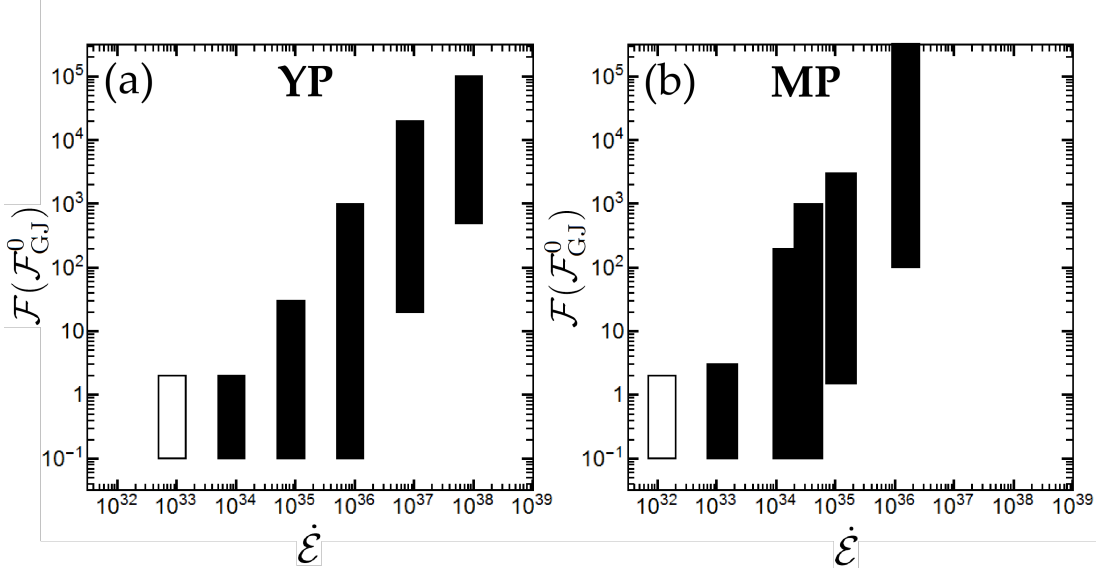


Figure 13. The \mathcal{F} value ranges that produce ϵ_{cut} values within the *Fermi* zone (see Fig. 12) as a function of $\dot{\mathcal{E}}$, in log-log scale. The rectangle widths denote the $\dot{\mathcal{E}}$ range (see Table 2) while the rectangle heights denote the optimum \mathcal{F} range. The black filled rectangles indicate models that produce ϵ_{cut} values within the *Fermi* zone while the white rectangles indicate models that fail to fall within the *Fermi* ϵ_{cut} values. In the latter case, the corresponding \mathcal{F} range (i.e. vertical dimension) denotes the \mathcal{F} values that produce ϵ_{cut} close to the *Fermi* zone. We see that for high $\dot{\mathcal{E}}$ YPs and MPs the optimum \mathcal{F} can reach up to 10^5 .

sponding to the different particle injection rates (\mathcal{F} ; see Table 1) that are denoted by the different colors according to the indicated color scale. We observe the presence of a maximum at $\log(E_0/E) \lesssim -2$ associated with a thermal-like particle distribution along with a bump that always appears in these distributions at higher values. The thermal-like maximum is related to the fluctuating (noisy) field behavior; its value depends primarily on the time-step and the number of macroparticles in our simulations. The higher value component (i.e. bump), beyond the vertical dashed line, actually indicates the magnetosphere regions where the true high acceleration takes place. We have checked that the E_0/E -position of the maximum decreases (increases) as we reduce (strengthen) noise. Thus, when we increase the number of macro-particles and/or decrease the time-step and/or increase the spatial resolution and/or increase the effective area of the current smoothing kernel the maximum of the distributions shown in Fig. 8 moves to lower $\log(E_0/E)$ values. In Fig. 8, the gradual drift of the maximum towards higher $\log(E_0/E)$ as \mathcal{F} increases is due to the corresponding poorer resolution for λ_D and ω_p (aka higher noise level). The increase of \mathcal{F} implies higher particle number densities and consequently smaller λ_D and higher ω_p . Keeping all the other parameters (e.g. d , dt) the same, these lower λ_D and higher ω_p values are more poorly resolved. This gradually enhances the noise leading to the increase of the position of the maximum. On the other hand, we see that the area under the non-thermal extension (i.e. bump) decreases with increasing \mathcal{F} . This implies smaller magnetosphere volumes with consistent accelerating electric field components and lower actual accelerating electric fields. Actually, Fig. 8 indicates also our limitations for the highest \mathcal{F} values we can use for a specific parameter set. Thus, as \mathcal{F} increases and the $\log(E_0/E)$ maximum moves towards higher val-

ues, the gradually reducing area under the bump eventually (at some \mathcal{F} value) is buried under the corresponding noise.

In Fig. 9 we show, in the indicated linear color scale, the $\log(E_0/E)$ values on the poloidal $\mu - \Omega$ plane for $\alpha = 45^\circ$ simulations and for the indicated \mathcal{F} values. The reddish regions denote the regions with values higher than the value corresponding to the dashed vertical line shown in Fig. 8. We see that at lower \mathcal{F} values large magnetosphere regions have consistent accelerating electric fields while for higher \mathcal{F} values the reddish regions shrink and finally are restricted to only near the ECS outside the LC. For all the model results presented below, we assume that the particle acceleration that produces the high-energy emission takes place in the magnetosphere regions corresponding to values greater than the one indicated by the dashed line in Fig. 8. We have decided to use the same threshold value for consistency even though the bump appears at slightly different values. However, we have checked that taking into account the regions corresponding to smaller $\log(E_0/E)$ values (for the simulations where the bump appears earlier than the dashed line in Fig. 8) do not change the results, mainly because the corresponding accelerating electric components are small. Moreover, we have seen that the ohmic $\mathbf{J} \cdot \mathbf{E}$ dissipation takes place largely in the magnetosphere regions corresponding to $\log(E_0/E)$ values higher than the dashed line threshold. For the rest of the magnetosphere the total $\mathbf{J} \cdot \mathbf{E}$ dissipation tends to zero.

Finally, we note that in real pulsar magnetospheres, the noise level (i.e. the maximum of the distribution in Fig. 8) is expected to be much smaller relative to the maximum of E_0/E in our simulations. This allows, in principle, the existence of consistent accelerating electric fields for much lower $\log(E_0/E)$ values than those we assume in our study. Nonetheless, these accelerating

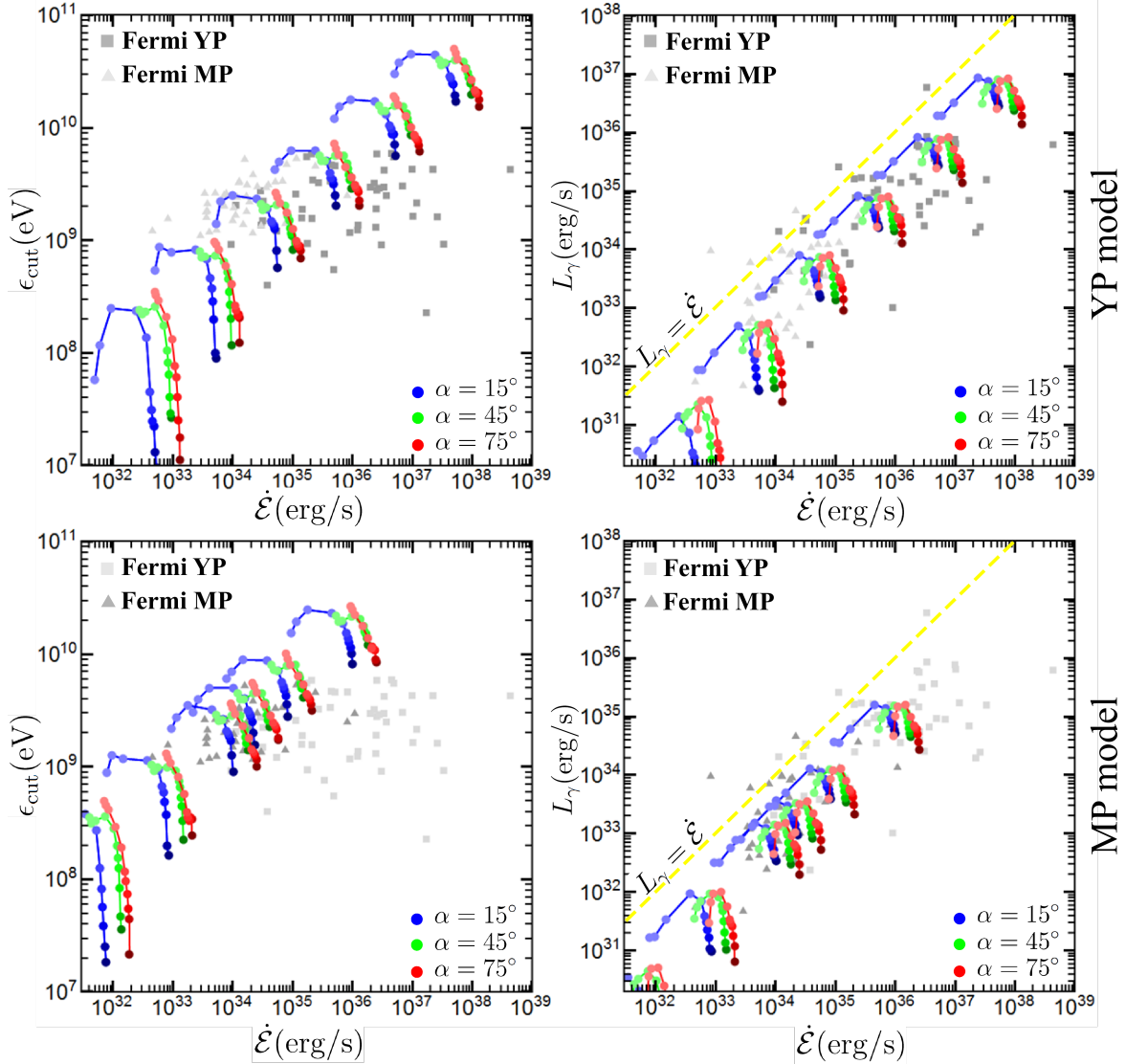


Figure 14. The model ϵ_{cut} values (left-hand column) and the model L_γ values (right-hand column) together with the corresponding *Fermi* ones (2PC) as a function of $\dot{\mathcal{E}}$ for YPs (top row) and MPs (bottom row). The blue, green, and red color denote simulations for $\alpha = 15^\circ$, $\alpha = 45^\circ$, and $\alpha = 75^\circ$, respectively. Each line-connected set of points corresponds to the same B_* and P values (see Table 2) while the darker the color hue the higher the corresponding \mathcal{F} value is. The *Fermi* data are denoted by gray rectangles (YPs) and triangles (MPs). The dashed yellow lines on the right-hand panels indicate 100% γ -ray efficiency (i.e. $L_\gamma = \dot{\mathcal{E}}$). The optimum \mathcal{F} ranges that produce ϵ_{cut} within the *Fermi* zone (see Figs. 12 and 13) reproduce the observed L_γ behavior (i.e. $L_\gamma \propto \dot{\mathcal{E}}$ for low $\dot{\mathcal{E}}$ and $L_\gamma \propto \sqrt{\dot{\mathcal{E}}}$ for high $\dot{\mathcal{E}}$). Our models imply that the observed L_γ dispersion could be the result of different \mathcal{F} values, different α values, and a variation of the beaming-factor, F_b , with the observer angle, ζ .

electric fields are expected to be important for the lower part of the emission spectrum (and not for energies near the ϵ_{cut} values observed by *Fermi*).

6. FITTING THE *FERMI* DATA

In real pulsars, the direct measurements of the period P and its derivative \dot{P} allow the calculation of the spin-down power. Assuming that the moment of inertia I is known the spin-down power is given by

$$\dot{\mathcal{E}} = \frac{4\pi^2 I \dot{P}}{P^3} \quad (9)$$

which can indirectly lead to an estimation of the magnetic field on the stellar surface. However, the spin-down power depends on the magnetosphere regime and is given by (Deutsch 1955; Spitkovsky 2006)

$$\dot{\mathcal{E}} = \frac{8\pi^4 r_*^6 B_*^2}{3c^3 P^4} \sin^2 \alpha \quad \text{for the VRD regime,} \quad (10a)$$

$$\dot{\mathcal{E}} = \frac{4\pi^4 r_*^6 B_*^2}{c^3 P^4} (1 + \sin^2 \alpha) \quad \text{for the FF regime.} \quad (10b)$$

By combining Eqs.(9), (10) we can get the B_* value with an uncertainty due to the unknown regime and the unknown α value. In the left (right) hand panel of

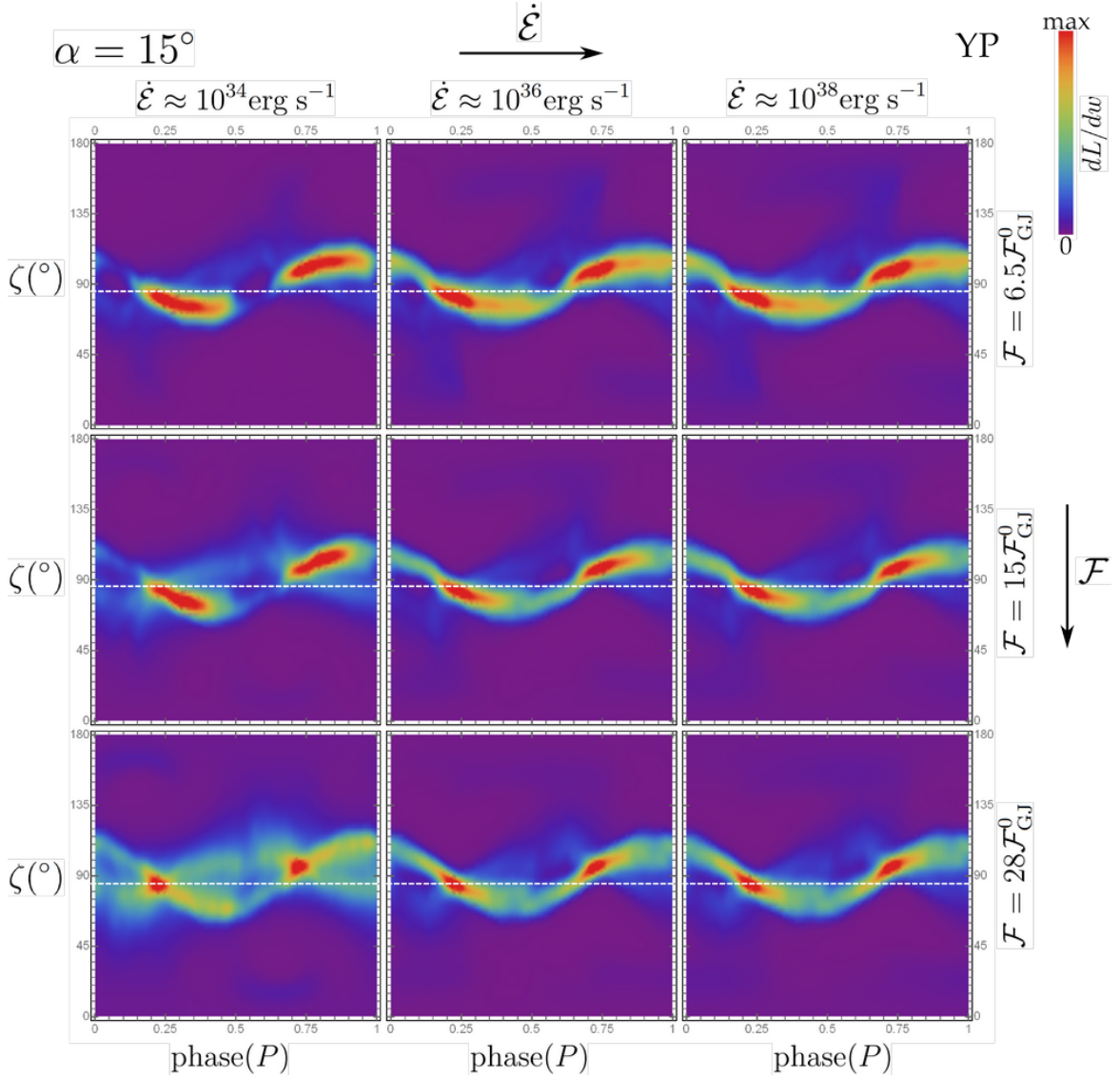


Figure 15. The sky-maps (i.e. luminosity per solid angle) for $\alpha = 15^\circ$ presented in the indicated linear color scale. Each column (row) corresponds to the indicated $\dot{\mathcal{E}}$ (\mathcal{F}) values. The white horizontal dashed lines indicate the ζ value that correspond to the light-curves shown in Fig. 19.

Fig. 10, we plot on (P, B_\star) diagrams all the *Fermi* YPs (MPs). Each pulsar is represented by a horizontal light gray line that denotes the uncertainty in B_\star estimation. We note that the left and right ends of the light gray lines denote the B_\star values that correspond to the $\alpha = 90^\circ$ at the FF and VRD regimes, respectively. The color stripes denote the indicated $\dot{\mathcal{E}}$ values using the same B_\star uncertainty as the light gray lines for the *Fermi* pulsars.

For the study of the high-energy emission in our simulations, we follow the approach that is discussed in the previous section. Table 2 shows the realistic P, B_\star values that we have chosen. The calculations described in the previous section are computationally demanding and therefore we have selected only 12 cases (6 for YPs and 6 for MPs) that trace well the corresponding observed area (see the black points in Fig. 10).

By calculating the realistic particle γ_R values, we can calculate not only the individual particle emissivity

($\propto \gamma_R^4 R_C^{-2}$; see Eq. 8) but also the entire CR spectrum of the corresponding emission. In Fig. 11, we plot, in log – log scale, the normalized distribution of the realistic γ_R values corresponding to a simulation with $\alpha = 45^\circ$ and $\mathcal{F} = 28F_{GJ}^0$. The top and bottom panels show the distributions for the different P, B_\star values that correspond to YPs and MPs, respectively.

Taking into account the emission from the entire magnetosphere (up to $2.5R_{LC}$) we construct the “global” spectrum, which we then fit with the model used in 2PC, namely,

$$\frac{dN}{d\epsilon} = A\epsilon^{-\Gamma} \exp\left(-\frac{\epsilon}{\epsilon_{\text{cut}}}\right) \quad (11)$$

where Γ is the photon-index.

Figure 12 shows, in log – log scale, the model ϵ_{cut} values as a function of the particle injection rates \mathcal{F} . The three different columns show the results for the indicated

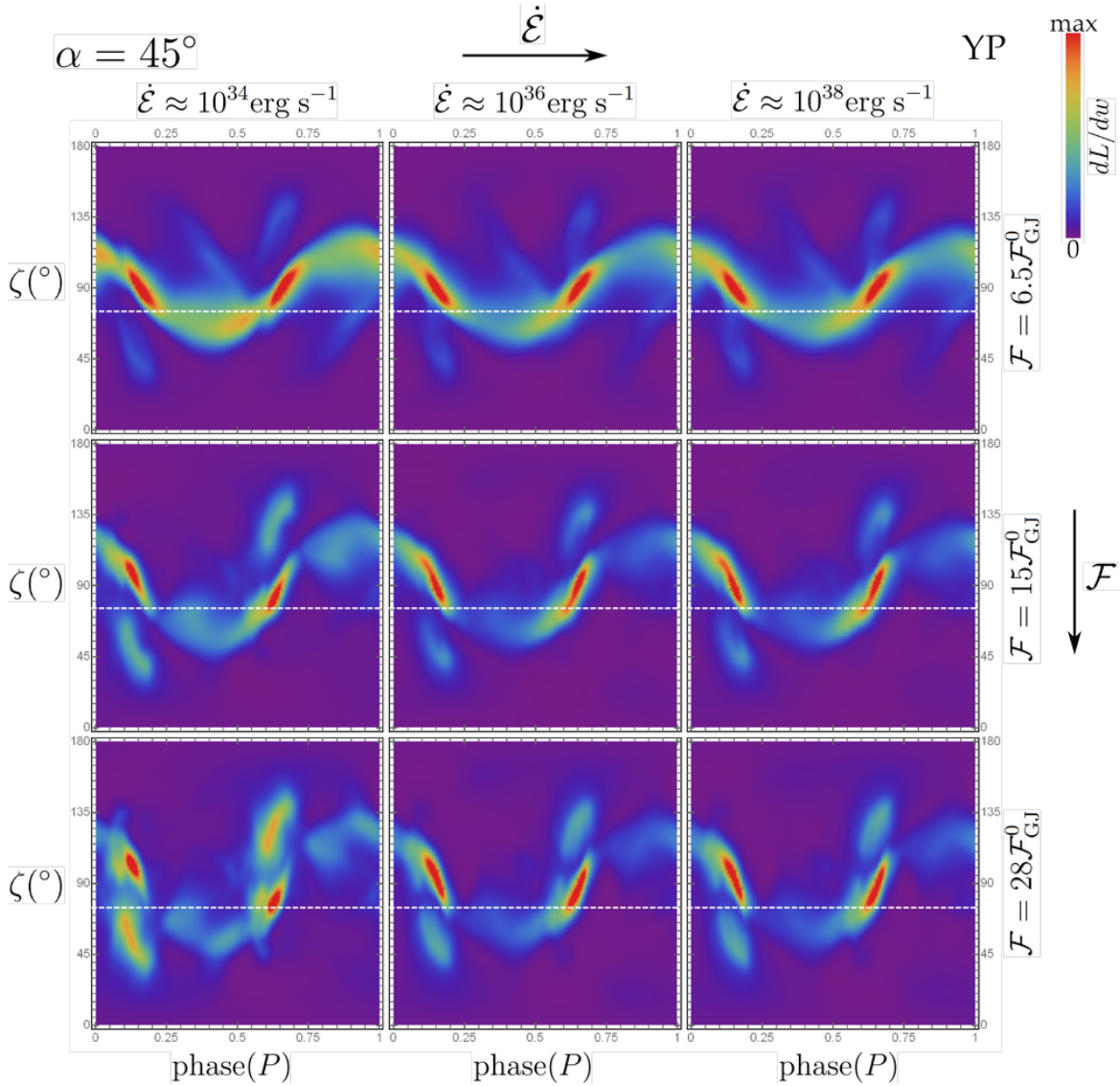


Figure 16. Similar to Fig. 15 but for $\alpha = 45^{\circ}$. The corresponding light-curves are shown in Fig. 20.

α values while the top and bottom rows show the results for the YP and MP model cases, respectively. The light greenish zones in each panel of Fig. 12 denote the zone of the observed (by *Fermi*) ϵ_{cut} values ($\sim 1 - 6 \text{ GeV}$). The different colors indicate the results for the different P , B_{\star} (i.e. $\dot{\mathcal{E}}$) values that are shown in Table 2. First, we see that, for the same \mathcal{F} value, the higher the $\dot{\mathcal{E}}$ the higher the corresponding ϵ_{cut} value. This increase is due to the corresponding higher accelerating electric components E_0 . We see also that for the same $\dot{\mathcal{E}}$ value (i.e. along a line) and for the high \mathcal{F} values ($\gtrsim 1\mathcal{F}_{\text{GJ}}^0$), ϵ_{cut} decrease with \mathcal{F} . This decrease is more prominent for low α and $\dot{\mathcal{E}}$ values. On the other hand, towards low \mathcal{F} values, ϵ_{cut} either decreases (for low α) or tends to stabilize (for high α). We have already discussed that low \mathcal{F} values produce solutions near VRD whose spin-down power (i.e. Poynting Flux), for low α values goes to very low values (see Eq. 10a). The low $\dot{\mathcal{E}}$ values imply a reservoir of low E fields and therefore low accelerating electric

components E_0 ($\leq E$). This is mainly the reason why, for low α values, ϵ_{cut} values decrease towards low \mathcal{F} .

Figure 12 provides a possible explanation for why we start observing YPs and MPs for spin-down powers $\gtrsim 10^{34} \text{ erg s}^{-1}$ and $\gtrsim 10^{33} \text{ erg s}^{-1}$, respectively. We see that for low \mathcal{F} values the low $\dot{\mathcal{E}}$ YP and MP models (see Table 2) struggle to reach the zone observed by *Fermi* ($\approx 1 \text{ GeV}$). Taking also into account now the *Fermi* threshold ($\approx 100 \text{ MeV}$) and the sensitivity of the instrument, we understand that YPs and MPs with $\dot{\mathcal{E}}$ values lower than those observed are difficult to be detected by *Fermi*. These objects, if they exist, should have spectra with ϵ_{cut} values lower than those observed by *Fermi* (at the MeV levels). We note here that all the MeV pulsars detected so far (Kuiper & Hermsen 2015) have high $\dot{\mathcal{E}}$ values. However, the light-curve characteristics of these objects indicate that the corresponding line-of-sight (i.e. ζ value) might not cross the core of the high-energy emission.

On the other hand, models with higher $\dot{\mathcal{E}}$ values lie

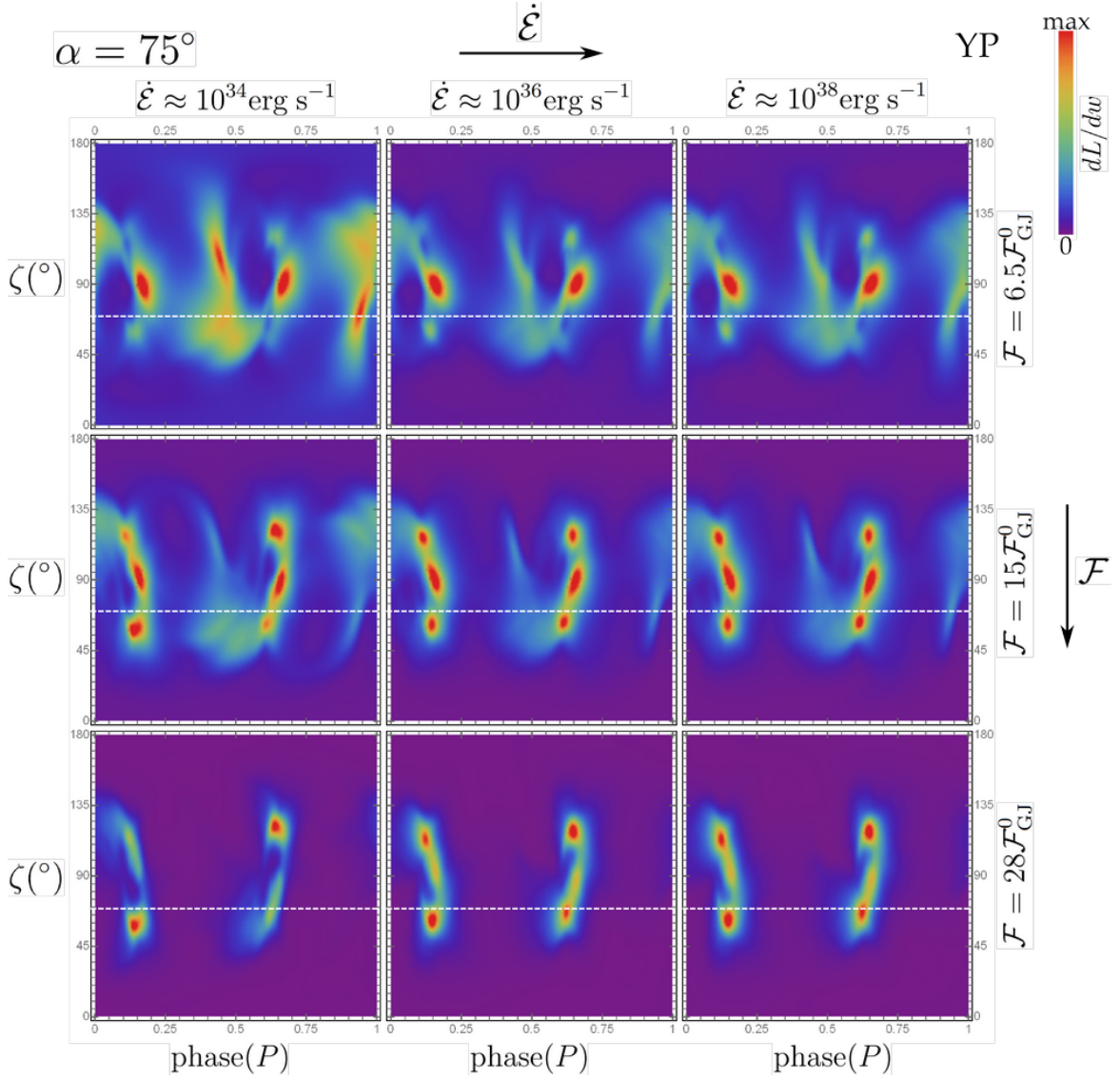


Figure 17. Similar to Fig. 15 but for $\alpha = 75^\circ$. The corresponding light-curves are shown in Fig. 21.

within the *Fermi* zone for a range of \mathcal{F} values adopted in the current study. We see also that the high $\dot{\mathcal{E}}$ models ($\gtrsim 10^{37} \text{erg s}^{-1}$ for YPs and $\gtrsim 10^{35} \text{erg s}^{-1}$ for MPs) require higher \mathcal{F} values than those we have applied. However, higher \mathcal{F} values are a computationally very demanding task and so we get an estimation of the corresponding \mathcal{F} values by linear extrapolations (see dashed lines in Fig. 12).

In Fig. 13, we plot, in log – log scale, the \mathcal{F} value as a function of $\dot{\mathcal{E}}$ that produces ϵ_{cut} values within the *Fermi* zone. Left (right) hand panel shows that results for YP (MP) models. The horizontal dimension of each rectangle denotes the model $\dot{\mathcal{E}}$ range (see Table 2) while the vertical dimension denotes the model \mathcal{F} range (for all α values) that provide ϵ_{cut} values within the *Fermi* zone. We note that for the optimum \mathcal{F} range we have taken into account the extrapolations shown in Fig. 12. The empty rectangles denote that no \mathcal{F} value can take the models within the *Fermi* zone. In this case the vertical \mathcal{F} range denotes the values that produce the closest to

the *Fermi* zone ϵ_{cut} values. We see that the highest \mathcal{F} for the high $\dot{\mathcal{E}}$ models can reach up to $10^5 - 10^6 \mathcal{F}_{\text{GJ}}^0$ which is consistent with the particle multiplicities found in local pair cascades studies (Timokhin & Harding 2015) and to the multiplicities that are needed for the explanation of the Crab nebula spectrum (de Jager et al. 1996).

In Fig. 14, we plot the ϵ_{cut} (left-hand column) and L_γ (right-hand column) values for all the YP (top row) and MP (bottom row) models together with the *Fermi* data, as functions of the corresponding spin-down power, $\dot{\mathcal{E}}$. We note that the darker the model points the higher the corresponding \mathcal{F} value. Similarly to Fig. 12, Fig. 14 reveals (from a different perspective than Fig. 12) the model \mathcal{F} value ranges that are consistent with both ϵ_{cut} and L_γ *Fermi* values. In the right-hand column, we see that a maximum appears as the \mathcal{F} varies from low to high values. This expected behavior reflects the ideal nature of the VRD and FF solutions. The former solutions have high fields but limited numbers of particles to dissipate the energy while the latter ones have high

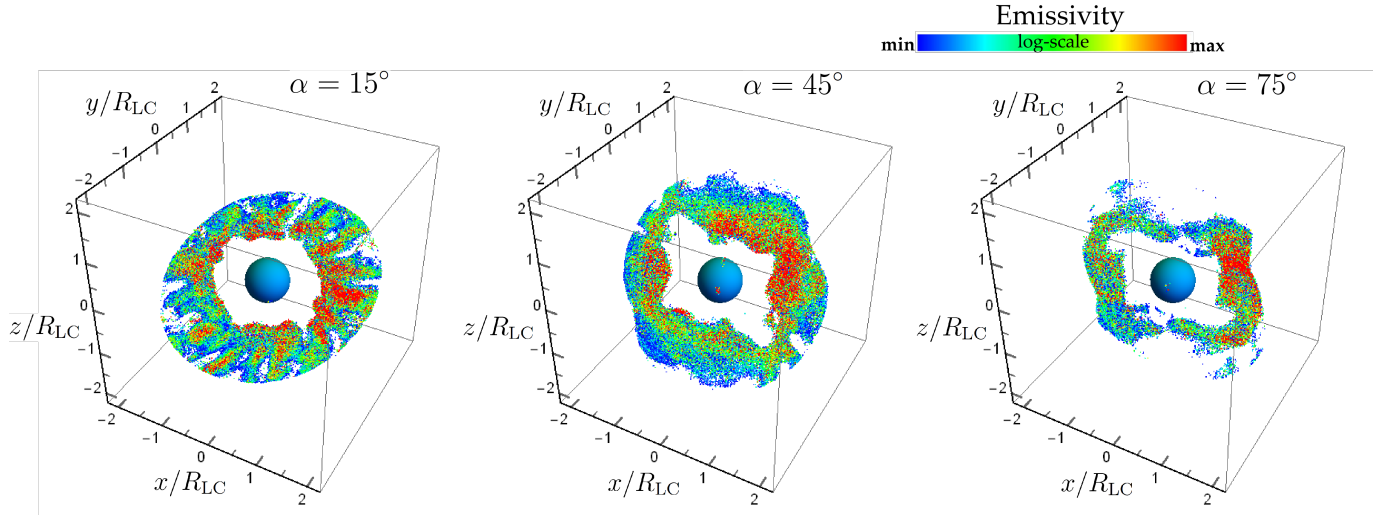


Figure 18. A random sample of the particles in the 3D space that produce the highest 95% of the observed radiated emission. The colors denote the emissivity according to the indicated logarithmic color scale. The max value indicated in the color scale is half an order of magnitude higher than the corresponding min one. The emission, for high α values, is not uniformly distributed in the ECS locus but it is more concentrated around the rotational equator. This effect had been originally seen in the macroscopic dissipative models (Kalapotharakos et al. 2014).

numbers of particles but limited energy available for dissipation. Taking into account the corresponding $\dot{\mathcal{E}}$ value, we see that the maximum efficiency ranges from $\approx 13\%$ to $\approx 35\%$ and is higher (lower) for the lower (higher) α values. We note that Fig. 14 implies that the optimum \mathcal{F} values that reproduce the 2PC L_γ values are somehow higher than the optimum \mathcal{F} values that reproduce the 2PC ϵ_{cut} values. Nonetheless, as we have discussed in (Kalapotharakos et al. 2017), the 2PC L_γ values are less reliable than the corresponding ϵ_{cut} values. The former ones depend on the assumed beaming-factor F_b and the estimated distances while their wide spread with $\dot{\mathcal{E}}$ indicates that other factors (i.e. α -values, variability of F_b with observer-angle, ζ) play an important role on their determination. On the other hand, the range of ϵ_{cut} values is more limited, it does not suffer from geometry or distance uncertainties, and depends weakly only on the adopted fit-model. A detailed study of the model F_b values that takes into account the observationally dependent parameters (e.g. α , ζ values, distances, instrument thresholds etc.) could eventually answer whether the observed γ -ray fluxes are consistent either with the model L_γ values corresponding to the optimum \mathcal{F} values that reproduce the observed ϵ_{cut} values or to the 2PC L_γ values, which assume always $F_b = 1$. Even though this study goes beyond the scope of the present paper, our preliminary calculations indicate that the average model F_b values are smaller than 1, which means, assuming the model correctness, that the 2PC L_γ values are overestimated. Finally, we note that the ϵ_{cut} of MPs for the same $\dot{\mathcal{E}}$ and \mathcal{F} are $\sim 3\times$ higher than the corresponding ones of YPs, which is consistent with the *Fermi* data (Kalapotharakos et al. 2017). This results from the $\epsilon_{\text{cut}} \propto B_\star^{-1/8}$ relation that is presented in Kalapotharakos et al. (2017) and emanates from the assumption that the emission takes place at the LC near the ECS due to CR at the radiation-reaction-limit-regime. Taking into account that $B_{\star\text{MP}} \approx 10^{-4} B_{\star\text{YP}}$ the

previous relation leads to $\epsilon_{\text{cutMP}} \approx 3\epsilon_{\text{cutYP}}$.

In Fig. 15, 16, and 17, we plot sky-map atlases for $\alpha = 15^\circ$, $\alpha = 45^\circ$, and $\alpha = 75^\circ$, respectively. In each figure, the different rows correspond to the different indicated particle injection rates (\mathcal{F}) while the different columns correspond to the indicated different YP models (i.e. different P , B_\star values and therefore different $\dot{\mathcal{E}}$ values; see Table 2). Each sky-map shows, in the indicated color scale, the emitted luminosity per solid angle ($dL/dw = dL/\sin(\zeta)d\zeta d\phi_{\text{ph}}$). The horizontal axis depicts the phase, ϕ_{ph} of the pulsar rotation while the vertical axis depicts the observer inclination angle, ζ , which is the angle between the rotational axis and the line of sight. Horizontal cuts of each sky-map correspond to the light-curve that is observed by an observer that lies at some ζ value. We note that the $\phi_{\text{ph}} = 0$ corresponds to the observed phase of photon that originates from the magnetic pole at $r \rightarrow 0$.

The sky-maps have been produced by collecting all the photons emitted by the particles from $t = 1.5P$ to $t = 2.0P$ (half a period). The simulations are in a steady state equilibrium during that time interval and therefore the photon collection from multiple time-steps (during this interval) reduces the noise considerably. The emissivity of each particle is considered $\propto \gamma_R^4 R_C^{-2}$ and the corresponding photon emission is along the particles' velocities. For the determination of the photon relative time of arrival (i.e. ϕ_{ph}) we take into account the corresponding relativistic time delay effects. Thus, ϕ_{ph} reads (see also Kalapotharakos et al. 2014))

$$\phi_{\text{ph}} = \left(\Omega t_S - \phi_{\mathbf{v}_p} - \frac{\mathbf{r}_p \cdot \mathbf{v}_p}{v_p} \frac{1}{R_{\text{LC}}} \right) \bmod 2\pi \quad (12)$$

where t_S is the global simulation time, $\mathbf{v}_p, \mathbf{r}_p$ are the particle velocity and position vectors, and $\phi_{\mathbf{v}_p}$ is the azimuth angle of the particle velocity \mathbf{v}_p with respect to the magnetic axis at $t_S = 0$ oriented according to $\mathbf{\Omega}$. The last term in Eq. (12) formulates the light travel time delay.

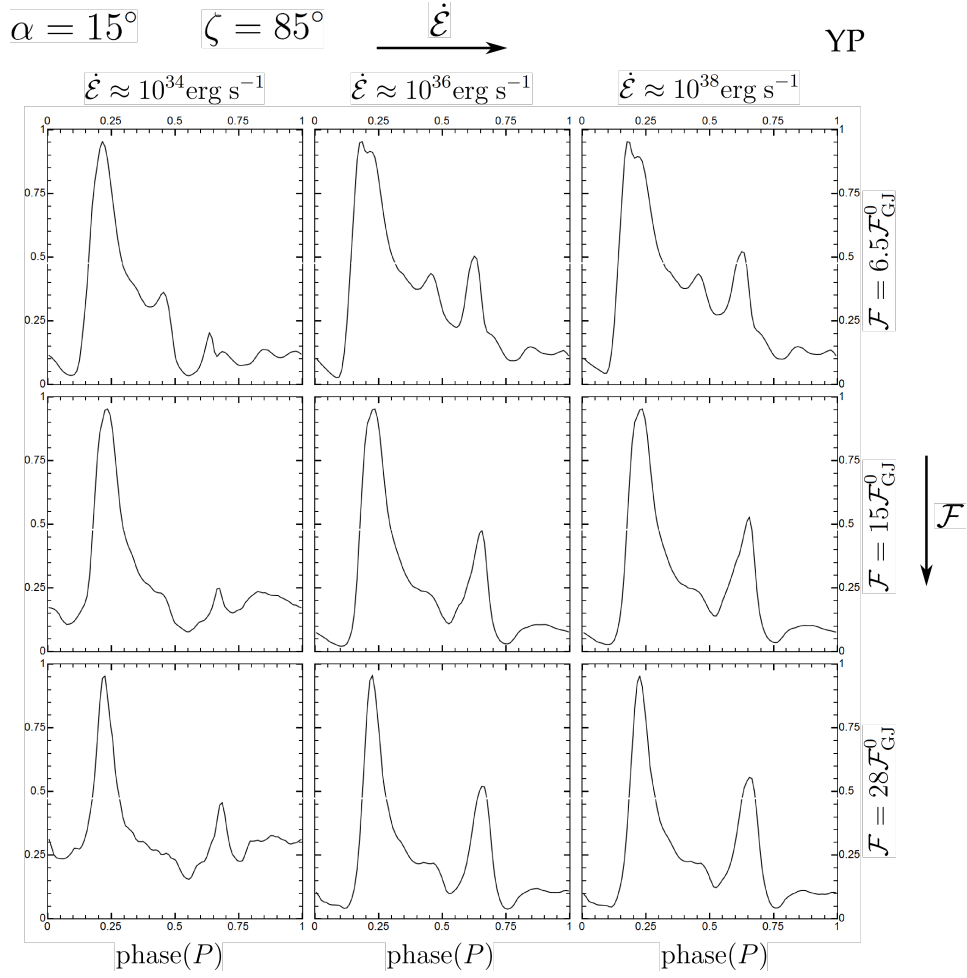


Figure 19. γ -ray light-curves for $\alpha = 15^\circ$. The plotted light-curves correspond to the ζ value ($\zeta = 85^\circ$) indicated by the horizontal white dashed line in Fig. 15.

The sky-map patterns actually are similar to those of the FIDO model (see fig. 17 of Kalapotharakos et al. 2014). For high inclination angles the locus of the ECS deviates considerably from the rotational equator allowing, in principle, the emission to contribute to very low and very high ζ values. However, in our models (of high α values), similarly to the FIDO models, the main part of the emission does not come from the high latitude (with respect to the rotational equator) zones. This makes the corresponding emission more concentrated around the rotational equator (i.e. around $\zeta = 90^\circ$).

Actually, in Fig. 18, we plot, for the indicated α values and for $\mathcal{F} = 20\mathcal{F}_{\text{GJ}}^0$, the particles that produce the highest 95% of the corresponding total L_γ value. The individual particle colors represent the corresponding emissivity as indicated in the color scale. The particle location is always near the ECS. However, we see that for low α values the particle distribution is quite uniform while for high α values most of the emission is produced by particles that are concentrated mainly closer (with respect to the theoretical extend) to the rotational equator. This behavior is similar to what had been originally noticed in the FIDO models (see fig. 19b of Kalapotharakos et al. 2014). A similar behavior is also seen in Cerutti et al. (2016). Figure 18 indicates also that for low α values the

emission is more concentrated near the LC while for high α values extends to larger distances (see the distribution of the red color points in Fig. 18).

Moreover, Figs. 15-17 indicate that towards high \mathcal{F} and $\dot{\mathcal{E}}$ values the luminous sky-map regions become narrower. This effect is further enhanced if we take into account that \mathcal{F} and $\dot{\mathcal{E}}$ increase together (see Fig. 13). This behavior is consistent with the observations, which show broader γ -ray light-curves towards low $\dot{\mathcal{E}}$ values of YPs and MPs (2PC).

In Figs. 19-21, we present, for demonstration, γ -ray light-curves for the indicated \mathcal{F} , α , $\dot{\mathcal{E}}$, and ζ values. These correspond to the ζ values indicated by the dashed white horizontal lines shown in Figs. 15-17. The γ -ray light-curves corresponding to high \mathcal{F} values appear very similar to the observed ones (2PC). As mentioned above, in these cases the sky-maps and the corresponding γ -ray light-curves are similar to the FIDO model ones and so they yield radio-lag values, δ , consistent with those indicated by *Fermi* (assuming that the radio emission comes from near the polar cap region).

However, we note that there are cases (mainly for low \mathcal{F} and high α values; see first rows of Fig. 17 and 21) that the light-curves seem to have more complicated features (e.g. more than two peaks, considerable inter-peak

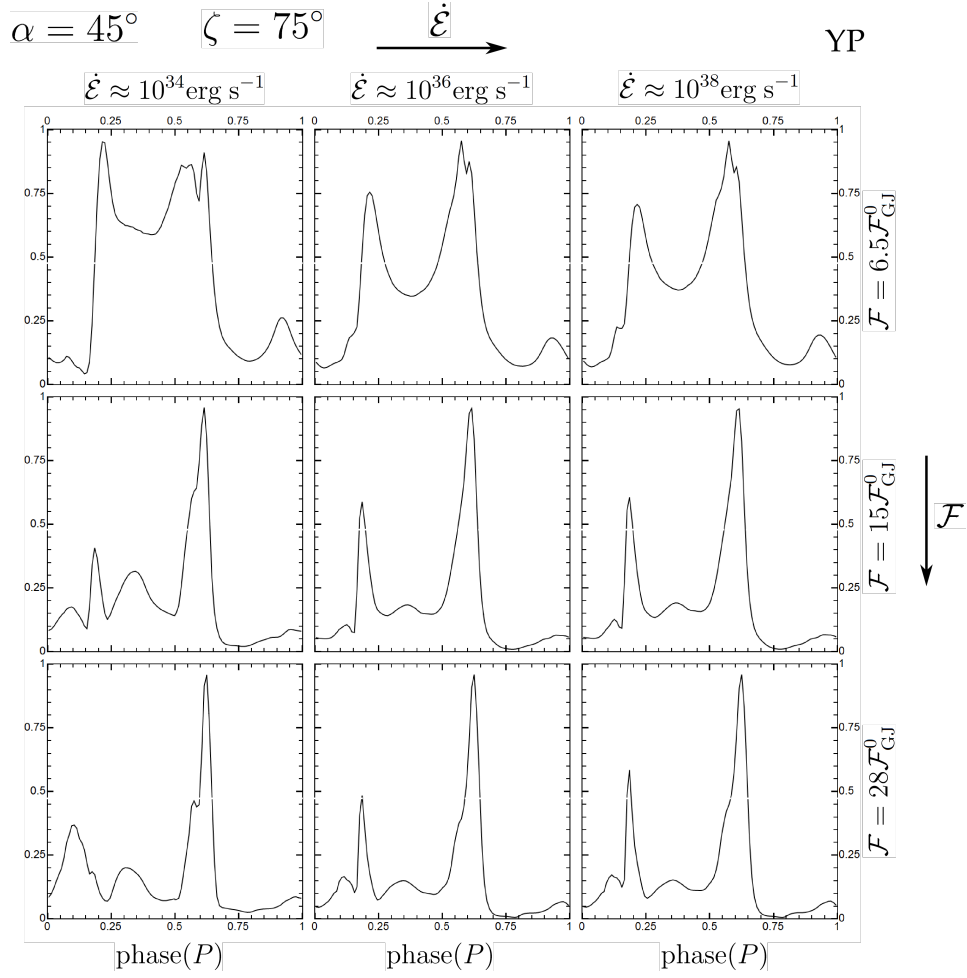


Figure 20. γ -ray light-curves for $\alpha = 45^\circ$. The plotted light-curves correspond to the ζ value ($\zeta = 75^\circ$) indicated by the horizontal white dashed line in Fig. 16.

and off-peak emission) not seen in the majority of the observed γ -ray light-curves. This is mainly due to the adopted “uniform”⁷ regulation of the particle injection rate. By reducing \mathcal{F} uniformly, we start introducing accelerating electric fields in regions (even inside the closed zone) that produce additional emission components not always consistent with the observed features. However, we note that peculiar and unique features in γ -ray light-curves exist in some MPs which have low $\dot{\mathcal{E}}$ value and are expected to be pair-starved (i.e. low \mathcal{F} values; see [Muslimov & Harding 2004](#); [Johnson et al. 2014](#)). Independently of this, it seems that the construction of realistic low \mathcal{F} models (i.e. weak pulsars, [Gruzinov 2013](#); [Contopoulos 2016](#)) should be made more carefully (compared to the approach followed in this study). Our results indicate that the observed γ -ray emission is regulated mainly by the particle abundance in regions near the ECS. For the rest of the magnetosphere regions the accelerating electric components are more easily screened and beyond some point (i.e. some \mathcal{F} value) no considerable emission is produced. Of course, the role of these regions might be important for the lower-energy part of the spectrum

(see also the related discussion in Section 5).

In Fig. 22, we plot, on the poloidal $\mu - \Omega$ plane, the origin of the particles (red for e^+ and blue for e^-) that eventually produce the highest 95% of the observed YP emission, in the case of $\mathcal{F} = 28\mathcal{F}_{\text{GJ}}^0$. We see that the particles that produce most of the observed emission are e^+ and originate along the separatrix. This particle population goes into the ECS, where it emits. A lower-energy population that originates mainly by the same locus regulates self-consistently the corresponding accelerating electric fields⁸. From all the above, it becomes apparent that an approach similar to what we followed in [Kalapotharakos et al. \(2017\)](#), becomes essential. In [Kalapotharakos et al. \(2017\)](#) (see also [Contopoulos et al. 2014](#)), we assumed that the dissipative region is only near the ECS beyond the LC and we applied the finite σ values only there. The equivalent in the PIC simulations would be to apply a rather high and constant particle injection rate in all the magnetosphere regions except for the ones indicated in Fig. 22. It seems that the regulation of only this population would provide results that are in full-agreement with the observations for the entire

⁷ The term uniform here implies just that the magnetization threshold in Eq. 4 is not magnetic field line dependent.

⁸ As we see in [Brambilla et al. \(2017\)](#) a drifting particle component can also contribute to the ECS.

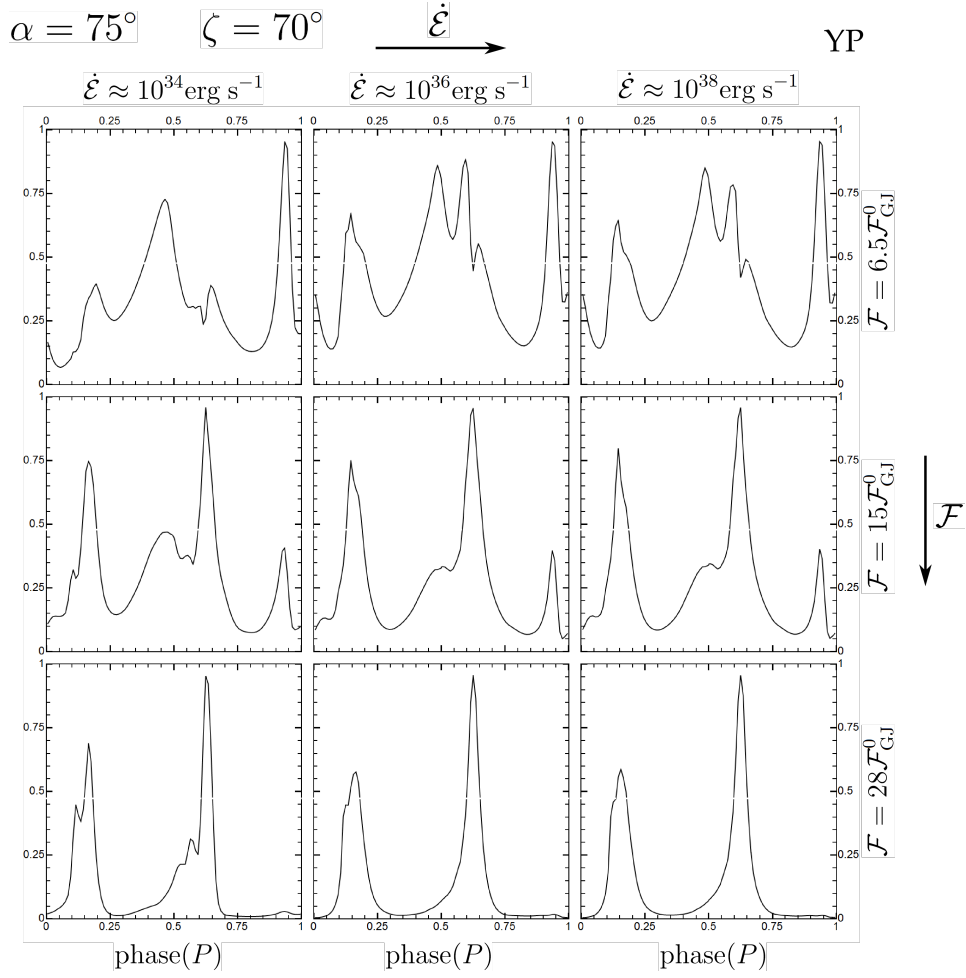


Figure 21. γ -ray light-curves for $\alpha = 75^\circ$. The plotted light-curves correspond to the ζ value ($\zeta = 70^\circ$) indicated by the horizontal white dashed line in Fig. 17.

range of the parameter space. This approach highlights the role of the return-current region in the high-energy emission observed in pulsars, something that, eventually, is expected to be supported by the (micro) physically motivated pair-creation.

7. CONCLUSIONS & DISCUSSION

In this paper, we present 3D kinetic global models of pulsar magnetospheres. In our study, we use C-3PA, an efficient, 3D cartesian relativistic Particle-In-Cell code we have developed. In this first step, we neglect the microphysics of the particle production and so we apply ad-hoc particle injection rates (\mathcal{F}) that at least produce pulsar magnetosphere models where the field structure and the corresponding particle distribution are consistent with each other (i.e. self-consistent).

The particle injection is applied up to large distances ($2.5R_{LC}$) and is regulated by the local magnetization. From low to high particle injection rates we cover an entire spectrum of solutions from near VRD to near FF, respectively. For models of high particle injection rates ($> 1\mathcal{F}_{GJ}^0$) the particle acceleration takes place mainly near the region of the equatorial current sheet outside the LC while the volume of this region decreases with the particle injection rate.

A main goal of this study is to uncover the properties of the model γ -ray emission and how these vary with the particle injection rate. However, in our PIC simulations the particle Lorentz factors are (due to numerical limitations) much smaller than those in real pulsar magnetospheres. Moreover, the relative way the synchrotron and curvature losses behave, can be quite different for different particle energy regimes. In our approach, we assume that the synchrotron losses in the environment of real pulsar magnetospheres rapidly reduce the corresponding pitch angles and so the synchrotron emission is not the main component of the observed γ -ray component. In our simulations, we use artificially scaled-up magnetic fields inside the radiation reaction force expressions in order to reduce the synchrotron cooling times. This affects mostly the geometry of the trajectories because of the suppressed gyro-motion. At the same time, along the PIC particle trajectories we derive realistic particle Lorentz factors by rescaling the fields and the length and time scales taking always into account the corresponding energy gain and the curvature radiation reaction losses. This approach allows the calculation of the corresponding high-energy emission (i.e. sky-maps, light-curves, spectra).

Using realistic value sets for the stellar surface mag-

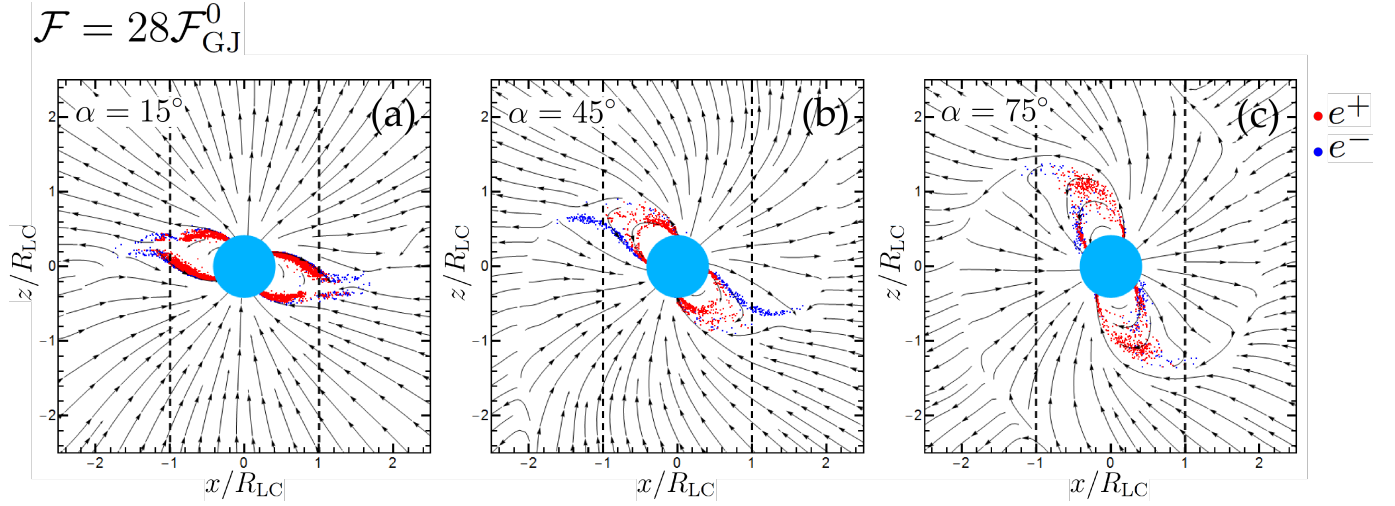


Figure 22. The origin of the charges (blue e^- , red e^+) on the $\mu - \Omega$ planes for the indicated α values that produce the highest 95% of the total emission for $\mathcal{F} = 28\mathcal{F}_{\text{GJ}}^0$.

netic field (B_\star) and period (P_s) that cover the corresponding observed value ranges of YPs and MPs, we find the following main results:

- (a) For the same particle injection rate, \mathcal{F} , the cutoff energies, ϵ_{cut} , increase with the spin-down power, $\dot{\mathcal{E}}$.
- (b) For the same B_\star and P_s values (i.e. $\dot{\mathcal{E}}$) the ϵ_{cut} decrease with \mathcal{F} for high \mathcal{F} and saturate for low \mathcal{F} .
- (c) The optimum \mathcal{F} values that produce ϵ_{cut} within the narrow value range observed by *Fermi* increase with $\dot{\mathcal{E}}$ and can reach up to 10^5 for both YPs and MPs. These optimum \mathcal{F} values produce also the observed L_γ behavior ($L_\gamma \propto \dot{\mathcal{E}}$ for low $\dot{\mathcal{E}}$ and $L_\gamma \propto \sqrt{\dot{\mathcal{E}}}$ for high $\dot{\mathcal{E}}$).
- (d) YP and MP models with $\dot{\mathcal{E}} \lesssim 10^{33} \text{ erg s}^{-1}$ and $\dot{\mathcal{E}} \lesssim 10^{32} \text{ erg s}^{-1}$ respectively produce ϵ_{cut} values that are always smaller than those observed by *Fermi* and close to the *Fermi* threshold, which provides a possible explanation for why we do not observe γ -ray YPs and MPs with smaller $\dot{\mathcal{E}}$.
- (e) The γ -ray efficiency shows a maximum (at $\mathcal{F} \approx 1.5\mathcal{F}_{\text{GJ}}^0$) that depends on the inclination angle, α , and ranges from 13% to 35%. For higher \mathcal{F} values the corresponding γ -ray efficiency drops considerably.
- (f) The higher the $\dot{\mathcal{E}}$ and \mathcal{F} , the more narrow the peaks in the γ -ray light-curves are.

For lower \mathcal{F} values (i.e. $\mathcal{F} \lesssim 10\mathcal{F}_{\text{GJ}}^0$), additional features begin appearing (especially for high α values) in the model γ -ray light-curves that are not always consistent with the observed ones. This indicates that the decrease of \mathcal{F} should not be uniform along all the magnetic field lines but more focused along the separatrix since these regions are the main suppliers of the particles that eventually lie in the region near the ECS. Actually, this is totally consistent with the approach we have followed for the FIDO models where the decrease of the plasma

conductivity σ was made only near the ECS and not in other places inside or outside the LC (Kalapotharakos et al. 2017). The above indicate that the number of particles that eventually enter the ECS region regulate the observed emission.

In Kalapotharakos et al. (2017) (FIDO models), we found a dependence of the plasma conductivity σ on $\dot{\mathcal{E}}$ while in the present study (kinetic models) we find a dependence of the global particle injection rate, \mathcal{F} on $\dot{\mathcal{E}}$ as well. Both these relations (σ vs. $\dot{\mathcal{E}}$ and \mathcal{F} vs. $\dot{\mathcal{E}}$) are imposed by the *Fermi* data and more specifically by the requirement that the models reproduce the observed ϵ_{cut} . Besides the ϵ_{cut} -success, the optimum FIDO and kinetic models provide very similar sky-maps and γ -ray light-curves that are consistent with the observed δ - Δ correlation while they reproduce the trends of the observed total γ -ray luminosity as a function of $\dot{\mathcal{E}}$. The apparent $\sigma - \mathcal{F} - \dot{\mathcal{E}}$ relation, uncovered by these studies, connects fundamental macroscopic quantities providing a unique insight into the understanding of the physical mechanisms behind the high-energy emission in pulsar magnetospheres. Nonetheless, this successful description eventually needs to be supported by the microphysical mechanisms that govern the particle creation processes providing eventually a complete justification for the aforementioned relations.

However, incorporating the pair creation microphysics (see Timokhin & Arons 2013) in global PIC simulations is not a trivial task because of the corresponding different length-time scales and the fact that the PIC energies are much smaller than those for real pulsars. Nonetheless, trying to expand our studies toward this direction, we have started exploring global magnetosphere models with magnetic field line dependent particle injection and fully self-consistent models that incorporate a physically motivated particle injection and we will present our results in forthcoming papers.

This work is supported by the National Science Foundation under Grant No. AST-1616632, by the NASA As-

trophysics Theory Program, by the NASA Astrophysics Data Analysis Program, and by Fermi Guest Investigator Program. Resources supporting this work were provided by the NASA High-End Computing (HEC) Program through the NASA Advanced Supercomputing (NAS) Facility at NASA Ames Research Center and NASA Center for Climate Simulation (NCCS) at NASA Goddard Space Flight Center.

REFERENCES

- Abdo, A., Ackermann, M., Atwood, W., et al. 2009, *ApJ*, 696, 1084 [1](#)
- Abdo, A., Ajello, M., Allafort, A., et al. 2013, *ApJS*, 208, 17 [1](#)
- Arka, I., & Dubus, G. 2013, *A&A*, 550, A101 [1](#)
- Arons, J. 1983, *ApJ*, 266, 215 [1](#)
- Arons, J., & Scharlemann, E. 1979, *ApJ*, 231, 854 [1](#)
- Bai, X.-N., & Spitkovsky, A. 2010, *ApJ*, 715, 1282 [1](#)
- Belyaev, M. A. 2015a, *MNRAS*, 449, 2759 [1](#)
- . 2015b, *New A*, 36, 37 [1](#)
- Berenger, J. 1996, *Journal of Computational Physics*, 127, 363 [2](#)
- Birdsall, C., & Langdon, A. 1991, *Plasma Physics via Computer Simulation* [2, 2](#)
- Bogovalov, S. 1999, *A&A*, 349, 1017 [1](#)
- Brambilla, G., Kalapotharakos, C., Harding, A., & Kazanas, D. 2015, *ApJ*, 804, 84 [1](#)
- Brambilla, G., Kalapotharakos, C., Timokhin, A., Harding, A. K., & Kazanas, D. 2017, submitted, *ArXiv* [1, 4, 8](#)
- Cao, G., Zhang, L., & Sun, S. 2016, *MNRAS*, 461, 1068 [1](#)
- Cao, G., Zhang, L., & Sun, S. 2016, *MNRAS*, 455, 4267 [1](#)
- Cerutti, B., Philippov, A., Parfrey, K., & Spitkovsky, A. 2015, *MNRAS*, 448, 606 [1, 5](#)
- Cerutti, B., Philippov, A., & Spitkovsky, A. 2016, *MNRAS*, 457, 2401 [1, 2, 6](#)
- Chen, A., & Beloborodov, A. 2014, *ApJL*, 795, L22 [1](#)
- Cheng, K., Ho, C., & Ruderman, M. 1986, *ApJ*, 300, 500 [1](#)
- Contopoulos, I. 2016, *MNRAS*, 463, L94 [6](#)
- Contopoulos, I., & Kalapotharakos, C. 2010, *MNRAS*, 404, 767 [1](#)
- Contopoulos, I., Kalapotharakos, C., & Kazanas, D. 2014, *ApJ*, 781, 46 [6](#)
- Contopoulos, I., Kazanas, D., & Fendt, C. 1999, *ApJ*, 511, 351 [1](#)
- Daugherty, J., & Harding, A. 1982, *ApJ*, 252, 337 [1](#)
- . 1996, *ApJ*, 458, 278 [1](#)
- de Jager, O. C., Harding, A. K., Michelson, P. F., et al. 1996, *ApJ*, 457, 253 [6](#)
- Deutsch, A. 1955, *Annales d'Astrophysique*, 18, 1 [1, 6](#)
- Goldreich, P., & Julian, W. 1969, *ApJ*, 157, 869 [1](#)
- Gruzinov, A. 2005, *Physical Review Letters*, 94, 21101 [1](#)
- . 2008, *ArXiv e-prints*, *arXiv:0802.1716* [5](#)
- . 2012, *ArXiv e-prints*, *arXiv:1205.3367* [5](#)
- Gruzinov, A. 2013, *ArXiv e-prints*, *arXiv:1303.4094* [6](#)
- Harding, A., & Kalapotharakos, C. 2015, *ApJ*, 811, 63 [5](#)
- Harding, A., Stern, J., Dyks, J., & Frackowiak, M. 2008, *ApJ*, 680, 1378 [5](#)
- Hewish, A., Bell, S., Pilkington, J., Scott, P., & Collins, R. 1968, *Nature*, 217, 709 [1](#)
- Hirotani, K., & Shibata, S. 2001, *MNRAS*, 325, 1228 [1](#)
- Johnson, T. J., Venter, C., Harding, A. K., et al. 2014, *ApJS*, 213, 6 [6](#)
- Kalapotharakos, C., & Contopoulos, I. 2009, *A&A*, 496, 495 [1, 2](#)
- Kalapotharakos, C., Contopoulos, I., & Kazanas, D. 2012a, *MNRAS*, 420, 2793 [1](#)
- Kalapotharakos, C., Harding, A., & Kazanas, D. 2014, *ApJ*, 793, 97 [1, 18, 6, 6](#)
- Kalapotharakos, C., Harding, A., Kazanas, D., & Contopoulos, I. 2012b, *ApJL*, 754, L1 [1](#)
- Kalapotharakos, C., Harding, A. K., Kazanas, D., & Brambilla, G. 2017, *ApJ*, 842, 80 [1, 6, 6, 7](#)
- Kalapotharakos, C., Kazanas, D., Harding, A., & Contopoulos, I. 2012c, *ApJ*, 749, 2 [1](#)
- Komissarov, S. 2006, *MNRAS*, 367, 19 [1](#)
- Krause-Polstorff, J., & Michel, F. C. 1985, *MNRAS*, 213, 43P [4](#)
- Kuiper, L., & Hermsen, W. 2015, *MNRAS*, 449, 3827 [6](#)
- Landau, L., & Lifshitz, E. 1987, *The classical theory of fields* [2](#)
- Li, J., Spitkovsky, A., & Tchekhovskoy, A. 2012, *ApJ*, 746, 60 [1, 5](#)
- Lyubarskii, Y., & Petrova, S. 1998, *A&A*, 337, 433 [5](#)
- Lyubarskii, Y. E. 1996, *A&A*, 311, 172 [1](#)
- McKinney, J. 2006, *MNRAS*, 368, L30 [1](#)
- Muslimov, A., & Harding, A. 2003, *ApJ*, 588, 430 [1](#)
- . 2004, *ApJ*, 606, 1143 [1, 6](#)
- Parfrey, K., Beloborodov, A., & Hui, L. 2012, *MNRAS*, 423, 1416 [1](#)
- Pétri, J. 2012a, *MNRAS*, 424, 2023 [1](#)
- . 2012b, *MNRAS*, 424, 605 [1](#)
- Pétri, J., & Kirk, J. 2005, *ApJL*, 627, L37 [1](#)
- Philippov, A., & Spitkovsky, A. 2014, *ApJL*, 785, L33 [1, 2](#)
- Philippov, A., Spitkovsky, A., & Cerutti, B. 2015a, *ApJL*, 801, L19 [1](#)
- Philippov, A. A., Cerutti, B., Tchekhovskoy, A., & Spitkovsky, A. 2015b, *ApJL*, 815, L19 [1](#)
- Philippov, A. A., & Spitkovsky, A. 2017, *ArXiv e-prints*, *arXiv:1707.04323* [1](#)
- Romani, R. 1996, *ApJ*, 470, 469 [1](#)
- Scharlemann, E., & Wagoner, R. 1973, *ApJ*, 182, 951 [1](#)
- Spitkovsky, A. 2006, *ApJL*, 648, L51 [1, 6](#)
- Spitkovsky, A., & Arons, J. 2002, in *Astronomical Society of the Pacific Conference Series*, Vol. 271, *Neutron Stars in Supernova Remnants*, ed. P. O. Slane & B. M. Gaensler, 81 [2, 4](#)
- Sturrock, P. A. 1971, *ApJ*, 164, 529 [1](#)
- Tamburini, M., Pegoraro, F., Di Piazza, A., Keitel, C. H., & Macchi, A. 2010, *New Journal of Physics*, 12, 123005 [2](#)
- Tchekhovskoy, A., Spitkovsky, A., & Li, J. 2013, *MNRAS*, 435, L1 [1](#)
- Timokhin, A. 2006, *MNRAS*, 368, 1055 [1](#)
- Timokhin, A., & Arons, J. 2013, *MNRAS*, 429, 20 [7](#)
- Timokhin, A., & Harding, A. 2015, *ApJ*, 810, 144 [6](#)
- Uzdensky, D. A., & Spitkovsky, A. 2014, *ApJ*, 780, 3 [5](#)
- Vay, J.-L. 2008, *Physics of Plasmas*, 15, 56701 [2](#)
- Villasenor, J., & Buneman, O. 1992, *Computer Physics Communications*, 69, 306 [2](#)